Magnetospheric Equilibrium with Anisotropic Pressure

By

PPPL--2762

DE91 015379

C. Z. Cheng

Princeton Plasma Physics Laboratory
Princeton University, Princeton, New Jersey 08543

Abstract

Self-consistent magnetospheric equilibrium with anisotropic pressure is obtained by employing an iterative metric method for solving the inverse equilibrium equation in an optimal flux coordinate system. A method of determining plasma parallel and perpendicular pressures from either analytic particle distribution or particle distribution measured along the satellite's path is presented. The numerical results of axisymmetric magnetospheric equilibrium including the effects of finite beta, pressure anisotropy, and boundary conditions are presented for a bi-Maxwellian particle distribution. For the isotropic pressure cases, the finite beta effect produces an outward expansion of the constant magnetic flux surfaces in relation to the dipole field lines, and along the magnetic field the toroidal ring current is maximum at the magnetic equator. The effect of pressure anisotropy is found to further expand the flux surfaces outward. Along the magnetic field lines the westward ring current can be peak away from the equator due to an eastward current contribution resulting from pressure anisotropy. As pressure anisotropy increases, the peak westward current can become more singular. The outer boundary flux surface has significant effect on the magnetospheric equilibrium. For the outer flux boundary resembling dayside compressed flux surface due to solar wind pressure, the deformation of the magnetic field can be quite different from that for the outer flux boundary resembling the tail-like flux surface.

1. Introduction

The perpetual presence of the energetic particles trapped in the magnetosphere and their ensuing magnetic drift motion in the geomagnetic field give rise to the ring current. Satellite measurements of the energy density of the ring current particle population indicate that the ring current plasma beta ($\beta = 2P/B^2$, where P is the plasma pressure and B is the magnetic field strength) may increase from about 10% during quiet periods to unity during intense geomagnetic storm times. The enhancement of the ring current is the result of solar wind interaction with the magnetosphere that allows some solar wind particles to penetrate into the tail region and to subsequently magnetic (gradient B and curvature) drift into the ring current region. This ring current plays the central role in deforming the earth's dipole field and results in the depression of geomagnetic field. In magnetospheric equilibrium model, plasma currents result from the requirement of force balance rather than being empirically prescribed. A good knowledge of the self-consistent magnetospheric equilibrium will provide physical insight into the internal structure of the magnetosphere. It will greatly improve our understanding of the satellite measurements of the magnetic field, particle flux, and plasma current. The accurate stability calculation of Alfvén wave instabilities such as mirror instability and ballooning mode depends sensitively on the local equilibrium quantities such as pressure anisotropy, pressure gradient, and magnetic field curvature [Cheng and Lin, 1987]. Problems of wave propagation, field line resonance, and particle orbit calculation that simulates the particle transport in the ring current region, also crucially rely on the knowledge of the equilibrium magnetic field.

The problem of computing the finite beta, static magnetospheric equilibrium has attracted much attention from the early days of space physics research. A successive iteration procedure has been adopted to solve the magnetohydrodynamic (MHD) momentum balance equation for the ring current magnetic field [Akasofu and Chapman, 1961; Hoffman and Bracken, 1965, 1967; Berko et al., 1975; Zavriyev and Hasegawa, 1990] on the basis of model current distribution. By prescribing an analytic form of the ring current particle distribution and choosing a magnetic field model as the initial approximation, the ring current perpendicular to the magnetic field was calculated from the momentum balance equation. The parallel ring current is assumed to be zero. The iterated magnetic field is then computed from the Biot-Savart law. The iteration procedure is usually stopped at the third iteration because large amount of computing is required and accuracy is difficult to obtain. By employing the pressure obtained from the particle distribution measured by the Active Magnetospheric Particle Tracer Explorers (AMPTE) CCE spacecraft, Lui et al. [1987] used the same successive iteration procedure, but with curvature current contribution from dipole field model, to compute the perpendicular ring current. Implicitly assumed in these studies is the

axisymmetric condition, which is in general not correct for storm time case. Another concern is the convergence of the iteration scheme, which may require much more than three iterations. The experience in computing toroidal equilibrium indicates that the number of required iterations when solving the MHD equilibrium equation is usually in the order of 20 or more, even though the difference between successive iterations may be less than 1%.

The Grad-Shfranov equation for axisymmetric magnetospheric equilibrium with isotropic pressure has been studied by Ip and Voigt [1985] and Voigt [1986a, 1986b] for the magnetosphere of Uranus. These calculations assume that the pressure is proportional to the square of the magnetic flux so that the Grad-Shfranov equation becomes linear in the magnetic flux. Attempt was made [Hau and Voigt, 1990] to improve the quadratic pressure assumption for the calculation of the shape of the two-dimensional magnetotail. Numerical calculation of the two-dimensional near magnetotail equilibrium for anisotropic pressure was performed [Whipple et al., 1990] by integrating the Poisson equation for the component of the vector potential in the symmetry direction. The perpendicular current density in the Poisson equation was obtained by specifying an analytical bi-Maxwellian particle distribution function. These calculations were done only for the simplifying rectangular geometry.

Recently, mathematical representations of the electric current density and magnetic field were derived in anisotropic magnetohydrostatic plasma for which the particle motions parallel to the magnetic field are adiabatic [Heinemann, 1990]. An explicit expression for current density is obtained by solving the momentum equation, Ampere's law, and charge conservation for the current density. Their formulation neither provides more information than other formulations, nor offers any computational advantage. However, it provides some physical insight by expressing the field-aligned current in terms of an integration of the perpendicular plasma drift along the entire field line.

In the paper we present accurate numerical solutions of self-consistent magnetospheric plasma equilibrium with anisotropic pressure [Cheng, 1990]. The numerical method involves solving the inverse equilibrium equation by an iterative metric method [DeLucia et al., 1980]. Numerical studies are performed to show the effects of finite beta, pressure anisotropy, and boundary condition on the axisymmetric magnetospheric equilibrium. For the isotropic pressure cases, the finite beta effect produces outward expansion of the constant magnetic flux surfaces, and along the magnetic field the toroidal ring current is maximum at the magnetic equator. The effect of pressure anisotropy will further expand the flux surfaces outward in the low field region. Along the magnetic field lines the westward ring current can be peak away from the equator and becomes

more singular as pressure anisotropy increases. This suggests that, against common belief, the westward ring current can be peaked away from the equator in the magnetosphere. The conservation of particle energy and the adiabatic invariance of the magnetic moment dictate that trapped particles will have relatively larger perpendicular velocity and smaller parallel velocity in high magnetic field regions than in low field regions, the parallel pressure is enhanced in low field region accordingly to provide an outward shift of the constant parallel pressure surfaces with respect to the corresponding constant magnetic flux surfaces. Since the particles are trapped in the lower magnetic field region with larger perpendicular velocity than parallel velocity, the perpendicular pressure will be enhanced even more than the parallel pressure. The outer boundary flux surface has significant effect on the magnetospheric equilibrium. For the outer flux boundary resembling the dayside compressed flux surface due to solar wind pressure, the deformation of the magnetic field can be quite different from that for the outer flux boundary resembling the tail-like flux surface.

In Section 2, the problem of obtaining general magnetospheric equilibrium with anisotropic pressure is formulated. An optimal flux coordinate system is presented. An equilibrium equation is derived for axisymmetric magnetospheric equilibrium with anisotropic pressure. The boundary conditions are discussed. A method of determining plasma pressure from either analytic particle distribution or particle distribution measured along the satellite's path is presented. In Section 3, an inverse equilibrium problem is derived to allow for accurate solution of the magnetic flux function by an iterative metric method. The numerical results for axisymmetric magnetospheric equilibrium with the effects of finite beta, pressure anisotropy, and boundary condition are presented in Section 4. A summary of this paper and a discussion on future extension of this work to study three-dimensional magnetospheric equilibrium are given in Section 5.

2. Magnetospheric Equilibrium

2.1 *Anisotropic MHD Equilibrium Model*

If the plasma convection in the magnetosphere is small, the magnetospheric equilibrium can be approximated by a static MHD equilibrium with anisotropic pressure, which is described by the system of equations

$$\vec{J} \times \vec{B} = \nabla \cdot \vec{\vec{P}} = \nabla P_{\perp} - \nabla \cdot [(P_{\perp} - P_{\parallel}) \hat{b} \hat{b}] , \qquad (2.1)$$

$$\nabla \times \vec{B} = \vec{J}, \tag{2.2}$$

$$\nabla \cdot \vec{B} = 0, \tag{2.3}$$

where $\hat{b}$ is a unit vector along a magnetic field line, and $\vec{J}$, $\vec{B}$, and $\vec{\vec{P}}$ are the equilibrium current, magnetic field, and pressure tensor, respectively. $P_\perp$ and $P_\parallel$ are functions of magnetic flux function ψ and the magnitude of the magnetic field B. It is convenient to introduce the functions

$$\sigma \equiv 1 + (P_\perp - P_\parallel)/B^2, \tag{2.4}$$

and

$$\tau \equiv 1 + (1/B)(\partial P_\perp/\partial B)_\psi. \tag{2.5}$$

If $\sigma > 0$ and $\tau > 0$ are satisfied everywhere in the plasma, the magnetosphere is stable to the well-known MHD "firehose" and "mirror" instabilities, respectively [Grad, 1967]. Equation (2.1) can be rewritten as

$$\sigma \vec{J} \times \vec{B} = \nabla P_\perp - (\vec{B} \cdot \nabla \sigma)\vec{B} + (1-\sigma)\nabla (B^2/2). \tag{2.6}$$

From Eq. (2.6), the momentum balance equation parallel to the equilibrium magnetic field is given by

$$\vec{B} \cdot \nabla P_\parallel = (P_\parallel - P_\perp)\, \hat{b} \cdot \nabla B, \tag{2.7}$$

and the momentum balance equation perpendicular to the magnetic field is given by

$$\nabla_\perp (B^2/2 + P_\perp) = \vec{\kappa}\, \sigma B^2, \tag{2.8}$$

where $\vec{\kappa} = \hat{b} \cdot \nabla \hat{b}$ is the magnetic field curvature. From Eq.(2.7), σ can be expressed as $\sigma = 1 - (1/B)(\partial P_\parallel/\partial B)_\psi$.

2.2 Coordinate System

Considerable thought should be given to the choice of coordinate system adopted for the calculation. From the numerical point of view, an improper choice could introduce the need for a considerable interpolation with its concomitant introduction of error. A wise choice of a natural coordinate system for the magnetospheric magnetic field can considerably increase the computational efficiency and accuracy.

For a general three dimensional magnetospheric equilibrium with nested flux surfaces, the magnetic field can be expressed as

$$\vec{B} = \nabla\psi \times \nabla\alpha \ , \tag{2.9}$$

where ψ is chosen as the magnetic flux function . Both ψ and α are constant along magnetic field lines. The lines where surfaces of constant ψ and α intersect represent magnetic field lines. Note that ψ must be a period function of toroidal angle ϕ in cylindrical (R, ϕ, Z) coordinate to ensure periodicity constraint. In terms of a flux coordinate system (ψ,ϕ,χ) with χ is the generalized poloidal angle varying between 0 and 2π, α can be expressed as $\alpha = \phi - q(\psi)\,\chi - \delta(\psi,\phi,\chi)$ without loss of generality, where $\delta(\psi,\phi,\chi)$ is periodic in both χ and ϕ. The flux coordinate system is in general not orthogonal and its metric is complicated because $\nabla\psi \bullet \nabla\chi \neq 0$, $\nabla\psi \bullet \nabla\phi \neq 0$, and $\nabla\phi \bullet \nabla\chi \neq 0$. A straight field line flux coordinate can be constructed by choosing $\zeta = \phi - \delta(\psi,\phi,\chi)$ to replace ϕ so that $\vec{B}\bullet\nabla\zeta \,/\, \vec{B}\bullet\nabla\chi = q(\psi)$. This feature is particularly useful since the operator $\vec{B}\bullet\nabla$ occurs frequently in the stability calculations. The Jacobian of the straight field line flux coordinate system is given by $\mathcal{J} = (\nabla\psi\times\nabla\zeta\bullet\nabla\chi)^{-1}$. The poloidal flux within a magnetic surface is $\Psi = \int d^3x\ \vec{B}\bullet\nabla\chi = (2\pi)^2\psi$. We note that computational study for general three-dimensional magnetospheric equilibrium in terms of the magnetic field representation, Eq.(2.9), is still in the early stage of development.

For a simplified axisymmetric magnetospheric equilibrium with nested flux surfaces, the magnetic field can be expressed as

$$\vec{B} = \nabla\psi \times \nabla\phi \, . \tag{2.10}$$

where ψ is a function of R and Z only. Since $\vec{B}\bullet\nabla\psi = \vec{B}\bullet\nabla\phi = 0$, the lines of the magnetic field and the lines of constant ψ coincide. A natural coordinate system is the flux coordinate system (ψ,ϕ,χ). Note that the flux coordinate system is in general not orthogonal with $\nabla\psi\bullet\nabla\chi \neq 0$. Along a flux surface in the poloidal plane we have

$$ds / d\chi = \boldsymbol{J} \ |\nabla\psi| \ / \ R \,, \tag{2.11}$$

where ds is the element of arc length along the magnetic field line. The specification of $\boldsymbol{J}$, therefore, determines the χ coordinate. By choosing $\boldsymbol{J}\ (R,Z) = \lambda(\psi)\, R \,/\, |\nabla\psi|$, where $\lambda(\psi)$ is given by the requirement that χ increases by 2π during one poloidal circuit, we have the equal arc length coordinate system.

2.3 Equilibrium Equation for Axisymmetric Magnetosphere with Anisotropic Pressure

In this paper we will limit our studies to axisymmetric magnetospheric equilibrium with nested flux surfaces. The $\nabla\phi$ component of Eq. (2.6) gives $\vec{J}\bullet\nabla\psi = 0$. The $\nabla\psi$ component of Eq. (2.6) leads to the toroidal ring current density

$$J_\phi = \ (R/\sigma)\,[\ (\partial P_\perp/\partial\psi)_B + \ (\tau - \sigma)\ (\nabla\psi\bullet\nabla B^2)\ /\ 2(\nabla\psi)^2\ ]\,. \tag{2.12}$$

The second term in Eq.(2.12) is due to pressure anisotropy and is responsible for the peaking of the ring current away from the equator along the field line. Since $\vec{J}\bullet\nabla\phi = \nabla\bullet(\vec{B}\times\nabla\phi) = -\nabla\bullet(\nabla\psi/R^2)$, and

$$\nabla\psi\bullet\nabla\sigma = \ (\nabla\psi)^2\ [\partial(P_\perp - P_\parallel)/\partial\psi]_B\ /\ B^2 + \ (\tau - \sigma)\ (\nabla\psi\bullet\nabla B^2)\ /\ 2B^2, \tag{2.13}$$

the anisotropic equilibrium equation [Grad, 1967] for axisymmetric equilibrium can be written in the familiar form

$$R^2\,\nabla\bullet(\nabla\psi\ /\ R^2) \ = \ -\ (1/\sigma)\ [\ R^2\ (\partial P_\parallel/\partial\psi)_B + \nabla\psi\bullet\nabla\sigma\ ]\,, \tag{2.14}$$

which will be used to solve for ψ if the functional form of $P_\parallel(\psi,B)$ and appropriate boundary conditions are specified. The isotropic limit of Equation (2.14) is obtained by setting $P_\perp = P_\parallel$, so

that $\sigma = 1$. In the vacuum case, the right hand side of Eq. (2.14) is identically zero. One of the vacuum solution is the dipole field with $\psi = -M \sin^2\theta / r$, where r and θ are the radius and polar angle in the spherical coordinate system (r,θ,ϕ), and M is the dipole moment. The components of the dipole magnetic field are given by $B_r = -2M \cos\theta / r^3$, and $B_\theta = -M \sin\theta / r^3$. Another vacuum solution is the uniform interplanetary magnetic field (IMF) along the Z-axis with $\psi = B_{IMF} R^2 / 2$, where B_{IMF} is the constant IMF.

It is important to consider the effect of pressure anisotropy to the ring current. Typically, both $(\tau - \sigma)$ and $[(\nabla\psi \bullet \nabla B^2) / (\nabla\psi)^2]$ are negative and decrease in magnitude along the field lines as one moves away from the equator. For example, $(\nabla\psi \bullet \nabla B^2) / (\nabla\psi)^2 = -6M (1 + \cos^2\theta) / r^5 (1 + 3 \cos^2\theta) < 0$ for a dipole field, and $(\tau - \sigma) = -(2P_\perp + P_\parallel)(P_\perp/P_\parallel - 1) / B^2 < 0$ for a bi-Maxwellian distribution. Since $(\tau - \sigma)$ decreases in magnitude faster than $[(\nabla\psi \bullet \nabla B^2) / (\nabla\psi)^2]$ along the field line away from the equator, from Eq.(2.12) one expects that pressure anisotropy contributes to a eastward current which is peaked at the equator.

2.4 Boundary Conditions

There are two ways to impose the boundary conditions in solving the equilibrium equation: the fixed boundary and the free boundary conditions. In the fixed boundary problem, the magnetic flux function ψ is specified at certain outer boundary of the computational domain such as the magnetopause. The magnetic boundary conditions at the magnetopause are usually specified either as closed or open [Toffoletto and Hill, 1986; Voigt, 1981, 1986b]. For the open magnetopause boundary condition, the magnetosphere and interplanetary magnetic field (IMF) lines are interconnected through the magnetopause. All the effects due to magnetopause current, tail current, IMF, and plasma outside the specified boundary are implicitly imposed through the specification of the boundary shape and it's assigned flux. In the free boundary problem, we have to employ a magnetospheric current loop systems [Olson and Pfitzer, 1977; Voigt, 1986b] to approximate the self-consistent magnetopause surface current and magnetotail current distributions. The shape of the magnetopause boundary consistent with the these current sources is then obtained as part of the solution.

In the paper we will consider the fixed boundary problem in solving the axisymmetric equilibrium equation. Since the plasma beta is insignificantly small for $r < 2R_E$ (R_E is the earth radius), the magnetic field is approximately a dipole field. Therefore, to reduce the computational domain and to avoid the singularity at $r = 0$, we will consider a computational domain bounded by

(a) an outer boundary with flux ψ_{out} and with shape to be specified, (b) an inner boundary with contribution due to dipole magnetic flux and IMF flux, and (c) boundary curves on the earth's surface between ψ_{in} and ψ_{out} curves. The choice of the outer boundary will take in account the effect of the solar wind [Mead and Beard, 1964; Toffoletto and Hill, 1986; Voigt, 1981, 1986b].

2.5 Anisotropic Pressure Distributions

In solving the equilibrium equation it is reasonable to specify the functional form of the two-dimensional parallel pressure $P_{\parallel}(\psi,B)$. The perpendicular pressure $P_{\perp}(\psi,B)$ is then determined from the parallel momentum balance equation, Eq.(2.7). A better way is to specify $\vec{\vec{P}}$ by prescribing the particle guiding center distribution for each species. For a collisionless plasma the particle energy ($\varepsilon = v^2/2$) and the adiabatic invariants, magnetic moment ($\mu = v_{\perp}^2/2B$) and the longitudinal invariant ($J_{\parallel} = \int ds\, v_{\parallel}$), are constant during the drift motions, where $v_{\parallel}$ and $v_{\perp}$ are the components of the velocity parallel and perpendicular to $\vec{B}$ respectively. The guiding center particle distribution function must have the form $F = F(\varepsilon,\mu,J_{\parallel})$. In general, $J_{\parallel} = J_{\parallel}(\varepsilon,\mu,\psi,\alpha)$ and $F = F(\varepsilon,\mu,\psi,\alpha)$, where ψ and α are related to the magnetic field through Eq.(2.9). If all particles on each field line share the same drift surface, where ψ labels the drift surface, then $J_{\parallel} = J_{\parallel}(\varepsilon,\mu,\psi)$ and $F = F(\varepsilon,\mu,J_{\parallel})$. With this form of particle distribution, the parallel and perpendicular pressures are given by

$$\begin{pmatrix} P_{\parallel} \\ P_{\perp} \end{pmatrix} = \sum_{j,\sigma_{\parallel}} 2\pi m_j \int_0^{\infty} d\varepsilon \int_0^{\varepsilon/B} d\mu \, [\, B\, F_j / |v_{\parallel}| \,] \begin{pmatrix} 2(\varepsilon - \mu B) \\ \mu B \end{pmatrix}, \tag{2.15}$$

where the summation is over the particle species j and $\sigma_{\parallel}$ which represents the direction of particle velocity parallel to $\vec{B}$, and m_j is the particle mass. The parallel velocity $v_{\parallel}$ has the form

$$v_{\parallel} = \sigma_{\parallel} \sqrt{2(\varepsilon - \mu B)} \ . \tag{2.16}$$

By inspection $P_{\perp}$ and $P_{\parallel}$ are functions of ψ and B only. Note that the parallel momentum balance equation, Eq. (2.7), is automatically satisfied if the particle distribution $F(\varepsilon,\mu,\psi)$ is used to compute $P_{\perp}$ and $P_{\parallel}$. The guiding-center particle distributions $F(\varepsilon,\mu,\psi)$ can be either prescribed by an analytical form or obtained from the satellite measurements of the particle flux. The particle

density and pressure everywhere along field lines can be integrated from an analytical distribution. For a bi-Maxwellian particle distribution $F(\varepsilon,\mu,\psi) = N(\psi)\,[2\pi T_{\parallel}(\psi)/m]^{-3/2}\,\exp[-m\varepsilon/T_{\parallel}(\psi) + m\mu B_o(\psi)/T_o(\psi)]$, the particle density is given by

$$n(\psi,B) = N(\psi)\,[T_{\perp}(\psi,B)\,/\,T_{\parallel}(\psi)] = N(\psi)\,[\,1 - B_o T_{\parallel}\,/\,B T_o\,]^{-1}, \tag{2.17}$$

the parallel pressure is given by

$$P_{\parallel}(\psi,B) = P(\psi)\,T_{\perp}(\psi,B)\,/\,T_{\parallel}(\psi), \tag{2.18}$$

the perpendicular pressure is given by

$$P_{\perp}(\psi,B) = P(\psi)\,[T_{\perp}(\psi,B)\,/\,T_{\parallel}(\psi)]^2, \tag{2.19}$$

and the pressure anisotropy parameter is given by

$$\tau = 1 + (2\,P_{\perp}\,/\,B^2)\,[\,1 - P_{\perp}\,/\,P_{\parallel}\,], \tag{2.20}$$

where $N(\psi)$ and $P(\psi) = N(\psi)T_{\parallel}(\psi)$ are the density and pressure in the isotropic limit, respectively. $B_o(\psi)$ can be chosen as the magnetic field at the magnetic equator. Other forms of analytical particle guiding center distributions [Longmire, 1963] have also been employed in previous calculations.

Although the measured particle distribution can only be obtained along a satellite's path, it can be used to construct the density and parallel pressure everywhere along field lines. Let $f(\varepsilon, v_{\parallel}/v, R)$ be the measured distribution along a satellite's path in the magnetic equatorial plane, where the magnetic field is assumed to be B_{min}(, the minimum value of $B(\psi,\chi)$ on each magnetic field line. Further assuming that B is a monotonically increasing function along a field line as one moves from the magnetic equator toward the earth, we can set

$$F(\varepsilon,\mu,\psi;B_{min}) = f(\varepsilon, v_{\parallel}/v, R). \tag{2.21}$$

The description can be extended to other value of $B(\psi,\chi)$ by choosing $F(\varepsilon,\mu,\psi;B) = F(\varepsilon,\mu,\psi;B_{min})$ if $B < \varepsilon/\mu$, and $F(\varepsilon,\mu,\psi,B) = 0$ if $B > \varepsilon/\mu$, since μ is a constant of motion. Thus the effect of mirroring of the particles as the magnetic field field increases is properly represented.

Since $\psi(R,Z)$ is the equilibrium solution, the assignment of $F(\varepsilon,\mu,\psi;B_{min})$ must be adjusted until it coincides with the measured particle distribution for all R values.

It is more accurate to convert back to $f(\varepsilon,v_{\parallel}/v,\psi)$ space at each value of ψ and B and compute the parallel pressure with

$$P_{\parallel}(\psi,B) = m \int d^3v\, v_{\parallel}^2\, f(\varepsilon,v_{\parallel}/v,\psi)\,, \tag{2.22}$$

because the distribution $f(\varepsilon,v_{\parallel}/v,\psi)$ is usually measured on uniform energy and pitch angle space grids. The perpendicular pressure can be determined in a similar way, but it is more accurate to use the parallel momentum balance equation, Eq.(2.7), to calculate it. From Eq.(2.7), we have

$$P_{\perp}(\psi,B) \equiv P_{\parallel}(\psi,B) - B\,(\partial P_{\parallel}/\partial B)_{\psi}\,. \tag{2.23}$$

If the satellite trajectory is not on the equatorial plane, a similar prescription can be formulated to construct the guiding center distribution $F(\varepsilon,\mu,\psi;B)$ from the particle distribution $f(\varepsilon,v_{\parallel}/v,R,Z)$ measured by satellites.

Recently significant progress has been made in the satellite observational data of ring current particle distribution from AMPTE/CCE [Lui et al., 1987] and ISEE 2 [Spence et al., 1989]. However, more complete information is required to give the full energy and pitch angle range and wider spatial coverage. More specifically, information of proton with energy between 1 and 25 keV, which is not presented in the earlier study by Lui et al. [1987], may be important. Lower charge states of oxygen ions, presumably injected from the ionosphere may have energy content as much as 30% of the total ring current energy, must be included. One of the future efforts will be to explore new satellite data of ring particle distribution as input to the self-consistent equilibrium calculation presented. The resultant equilibrium solution will be used to understand the magnetosphere phenomena.

3. Inverse Equilibrium Problem

In solving the anisotropic equilibrium equation one typically expresses the magnetic flux $\psi(R, Z)$ on a rectangular grid. However, for stability studies, it is not $\psi(R, Z)$ that is needed but rather the inverse functions $R(\psi,\chi)$ and $Z(\psi,\chi)$, where (ψ,χ) are generalized magnetic flux

coordinates with properties described in Sec. 2. To obtain these inverse functions numerically, one employs a mapping procedure to contour levels of constant ψ and χ. Thus, the (R,Z) coordinates of the intersection of the contours $\psi_i = i\,\delta\psi$ and $\chi_j = j\,\delta\chi$ form a discrete set of points $[R(\psi_i,\chi_j);\ Z(\psi_i,\chi_j)]$ which collectively define a finite difference approximation to the exact mapping $[R(\psi,\chi);\ Z(\psi,\chi)]$. The discrete mapping obtained in this manner is often adequate, but in general satisfies the flux coordinate form of the finite differenced equilibrium equation only to within some error introduced by truncation error in the original (R,Z) solution and in the contouring. The fact that this error is limited by the truncation error inherent in the finite difference equations rather than by an iteration tolerance (which can be made arbitrarily small) can render this method unacceptable for equilibrium with large local gradients of flux and current. A finite-difference method based on equal increments in (R,Z) space is not optimal for resolving these spatially local steep gradients.

To overcome these difficulties, we will consider solving the inverse equilibrium equation based on the flux coordinates instead of the equilibrium equation, Eq.(2.14). An iterative metric method will be used to solve for the discrete coordinate functions $[R(\psi,\chi);\ Z(\psi,\chi)]$ such that the flux coordinate form of the finite differenced inverse equilibrium equation based on these points is satisfied to an arbitrarily small tolerance. In addition, the numerical grid on which finite differences are evaluated is tied to the equilibrium solution itself in such a way that grid points automatically accumulate in regions of step gradients. We note that equilibrium containing separatrix or ergodic regions will not be found with the inverse equilibrium method unless provision is made to treat multiple regions and to match solutions where these regions meet.

3.1 Inverse Equilibrium Equation

To derive the inverse equilibrium equation in terms of a right-handed flux coordinates (ρ,ϕ,χ), where ρ labels magnetic surfaces of constant ψ, we note that

$$\mathcal{J}\ \nabla\bullet(\nabla\psi / R^2) = (\partial/\partial\rho)\,[\mathcal{J}\ \nabla\psi\bullet\nabla\rho / R^2] + (\partial/\partial\chi)\,[\mathcal{J}\ \nabla\psi\bullet\nabla\chi / R^2]\,. \quad (3.1)$$

The Jacobian $\mathcal{J} = (\nabla\rho\times\nabla\phi\bullet\nabla\chi)^{-1}$ can be expressed as derivatives of the cylindrical spatial coordinates (R, Z):

$$\mathcal{J} = R\,[\,(\partial R/\partial\rho)\,(\partial Z/\partial\chi) - (\partial R/\partial\chi)\,(\partial Z/\partial\rho)\,]\,. \quad (3.2)$$

In terms of the covariant representation in cylindrical coordinate, the vectors $\nabla\rho$ and $\nabla\chi$ can be expressed as

$$\nabla\rho = R\,[\,(\partial Z/\partial\chi)\,\nabla R - (\partial R/\partial\chi)\,\nabla Z\,]\,/\,\mathcal{J}\,, \tag{3.3}$$

and

$$\nabla\chi = R\,[\,(\partial R/\partial\rho)\,\nabla Z - (\partial Z/\partial\rho)\,\nabla R\,]\,/\,\mathcal{J}\,. \tag{3.4}$$

By defining $\psi = \psi(\rho)$ so that $\partial\psi/\partial\chi = 0$, the inverse equilibrium equation for axisymmetric magnetosphere is derived from Eqs.(2.13-14) and takes the form

$$\begin{aligned}&(\partial/\partial\rho)\,\{(\partial\psi/\partial\rho)\,[(\partial R/\partial\chi)^2 + (\partial Z/\partial\chi)^2]\,\mathcal{J}^{-1}\}\\ &-(\partial/\partial\chi)\,\{(\partial\psi/\partial\rho)\,[(\partial R/\partial\rho)(\partial R/\partial\chi) + (\partial Z/\partial\rho)(\partial Z/\partial\chi)]\,\mathcal{J}^{-1}\}\\ &= -\mathcal{J}\,\sigma^{-1}\{\,(\partial P_\perp/\partial\psi)_B + (\tau-\sigma)\,(\nabla\psi\bullet\nabla B^2)\,/\,2(\nabla\psi)^2\,\},\end{aligned} \tag{3.5}$$

which is regarded as an equation for the two-dimensional coordinate functions $R(\rho,\chi)$ and $Z(\rho,\chi)$. The Jacobian is chosen as

$$\mathcal{J} = R\,[\,(\partial R/\partial\rho)(\partial Z/\partial\chi) - (\partial R/\partial\chi)(\partial Z/\partial\rho)\,] = \lambda(\rho)\,R^m\,/\,|\nabla\rho|^n\,, \tag{3.6}$$

where m and n are arbitrary integers, so that (R, Z) is constrained. By appropriately choosing m and n, different nonorthogonal magnetic flux coordinate systems can be obtained. For the numerical solutions presented in Sec. 4 we choose m=n=1, which corresponds to an equal arc length coordinate along χ.

3.2 Iterative Metric Method

Numerically, an iterative metric method is employed [DeLucia et al., 1980] for solving the inverse equilibrium equation. An initial coordinate transformation corresponding to iteration level k=0 is guessed with $[R^{(k)}(i,j);\ Z^{(k)}(i,j)]$, where i = 1, N correspond to discrete ρ grids and j = 1, M correspond to discrete χ grids. The points corresponding to i = 1 define the inner plasma boundary and the points corresponding to i = N define the outer plasma boundary. The points corresponding to j = 1 and j = M define the boundary curves on the earth's surface between ψ_{in} and ψ_{out} curves. The finite difference form of the inverse equilibrium equation is then solved for

the magnetic flux function $\psi^{(k+1)}(i,j)$ at the new iteration level, k+1, using the coordinate transformation at the old iteration level, k, by the successive over-relaxation method [Roache, 1972]. To obtain the finite difference form of the inverse equilibrium equation, a center difference scheme is employed. The right hand side of the inverse equilibrium equation is evaluated at the old iteration level, k. Next, the coordinate functions at the new iteration level, $[R^{(k+1)}(i,j); Z^{(k+1)}(i,j)]$, are obtained from interpolation technique by using the magnetic flux function at the new iteration level, $\psi^{(k+1)}(i,j)$, so that the finite difference forms of the requirement that $\psi^{(k+1)}$ be constant along constant ρ surfaces and that the Jacobian constraint, Eq. (3.6), is satisfied; i.e., (1) $\partial\psi^{(k+1)}/\partial\chi = 0$, and (2) $R\,[(\partial R/\partial\rho)(\partial Z/\partial\chi) - (\partial R/\partial\chi)(\partial Z/\partial\rho)] = \lambda(\rho)\, R^m / |\nabla\rho|^n$ at the k+1 iteration level. The iteration procedure is repeated until the magnetic flux function is independent of χ and converges to some tolerance.

4. Numerical Results for Axisymmetric Magnetospheric Equilibrium

In the computational domain, the flux coordinates (ρ,ϕ,χ) are chosen with $0 \le \chi \le \pi$, $0 \le \phi \le 2\pi$, and $0 \le \rho \le 1$, where ρ is related to ψ by $\psi = -B_D R_o^3 / [R_{min} + \rho(R_{max} - R_{min})]$. The equatorial dipole magnetic field intensity is B_D at $R = R_o$. The magnetic flux is $\psi_{max} \equiv -B_D R_o^3 / R_{max}$ at the outer magnetic surface and is $\psi_{min} \equiv -B_D R_o^3 / R_{min}$ at the inner magnetic surface. The outer magnetic flux surface is specified by

$$\psi_{max} = -B_D R_o^3 \sin^2\theta / r + B_S (r - R_E)^2 \cos^2 3\theta, \qquad (4.1)$$

and the inner magnetic flux surface is given by

$$\psi_{min} = -B_D R_o^3 \sin^2\theta / r + B_I r^2 \sin^2\theta / 2. \qquad (4.2)$$

For positive values of B_S and B_I, the flux surface is compressed with respect to the dipole field surface. To enclose the computational domain, the boundaries are set on the earth's surface for $\psi_{min} \le \psi \le \psi_{max}$.

Rather than presenting a survey of anisotropic pressure magnetospheric equilibria with different particle distributions and pressure profiles, we shall concentrate on the effects of boundary condition, plasma beta, and pressure anisotropy. To generate the axisymmetric magnetospheric equilibrium, we need to specify the ring current plasma pressure profiles. In the

following we will employ the analytical anisotropic pressure, Eqs. (2.17)-(2.19), obtained from a bi-Maxwellian distribution with the P(ψ) profile given by

$$P(\psi) = P_o \left[(\psi_{max} - \psi)/\gamma \right]^{\gamma} \left[(\psi - \psi_{min})/\delta \right]^{\delta} \left[(\gamma + \delta)/(\psi_{max} - \psi_{min}) \right]^{\gamma+\delta}, \qquad (4.3)$$

where $T_o(\psi)$ and $T_{\parallel}(\psi)$ are chosen as constants, and $B_o(\psi)$ can be chosen as the magnetic field at the magnetic equator. Note that for $T_o >> T_{\parallel}$ the pressure is essentially isotropic.

In the followings we set $R_o = 6.6R_E$, $R_{min} = 2R_E$, $R_{max} = 10R_E$, $\gamma = 2$, $\delta = 2$, $B_D = 1$. Thus, the dipole magnetic field is normalized to be unity at $R = 6.6R_E$ in the equatorial plane. The plasma beta effect is studied by varying P_o, the effect of pressure anisotropy is studied by changing $(T_o/T_{\parallel})$, and the effect of boundary condition is studied by varying B_I and B_S.

4.1 Isotropic Pressure Case

Observed plasma pressure in the magnetosphere is almost always anisotropic. However, we will first study isotropic pressure cases to understand the effect of finite plasma beta by choosing a very large value of $(T_o/T_{\parallel})$, so that the pressure is practically isotropic and is a function of ψ only. For simplicity we set $(T_o/T_{\parallel}) = 10^4$ for all flux surfaces and varying P_o. The boundary condition parameters are set to be $B_I = B_S = 0$ so that the inner and outer flux surfaces are identical to the dipole field surfaces. The computation is performed for $P_o = 0.5$ with 50 flux surfaces and 61 poloidal angle grid points. The constant ψ contours are shown in Figure 1. The solid lines correspond to the equilibrium solution, and the dotted lines represent the dipole magnetic flux surfaces. In the low beta region the solid curves and dotted lines coincide for the same flux values. The effect of finite plasma beta is to shift the flux surface outward toward the lower magnetic field region, and is clearly shown in the large beta region (low field region) in Figure 1. This outward shift of flux surface is similarly observed in the tokamak equilibrium and is called Shfranov shift. The Shafranov shift is more pronounced for higher beta cases. The toroidal ring current contours are shown in Figure 2, which shows that along the magnetic field lines the ring current is peak at the equator. The dotted lines correspond to the equilibrium constant ψ surfaces. The ring current changes sign as one goes away from the earth; the current is eastward at small R and is westward at large R. The radial variations of the plasma pressure P, the plasma beta $\beta = 2P/B^2$, the toroidal ring current J_ϕ, and the percentage difference between the self-consistent magnetic field and dipole field $(B-B_D)/B_D$ in the equatorial plane are shown in Figures 3(a)-(d), respectively. Note that the maxima of P and β are located at different radial locations as shown in Figures 3(a) and 3(b). The peak pressure is located at $R = 3.3R_E$, and the peak beta is about 0.25 at $R \approx 7R_E$. Figure 3(c)

shows that the westward current is peaked at $R \approx 6.4R_E$, and the eastward current is peaked at $R \approx 2.5R_E$. This is consistent with analytical expression of the toroidal ring current given by $J_\phi = R(\partial P/\partial\psi)$; the most intense westward ring current can be several earth radii away from the location of maximum ring current pressure. Since $(\partial P/\partial\psi)$ is constant along the field line, J_ϕ is peak at the equator and decreases as the latitude increases toward the earth from the equator. The deformation of the magnetic field due to the ring current plasma pressure is shown in Figure 3(d); the magnetic field is reduced around the peak pressure gradient, $(\partial P/\partial\psi)$, location. The magnetic field deformation depends on the pressure profile and the boundary condition. For this case the magnetic field is reduced for $R < 7R_E$ and enhanced for $R > 7R_E$. For the same pressure profile and boundary condition the distortion of magnetic field is roughly proportional to the plasma beta for $P_o > 0.2$.

4.2 Anisotropic Pressure Case

To study the effect of pressure anisotropy on the magnetospheric equilibrium, we will vary $(T_o/T_{||})$ but set $B_I = B_S = 0$, $P_o = 0.5$. For simplicity we let $(T_o/T_{||})$ be independent of ψ. From Eqs. (2.18) and (2.19) we have $P_{||}(\psi,B)/P(\psi) = P_\perp(\psi,B)/P_{||}(\psi,B) = [1 - B_oT_{||} / BT_o]^{-1}$ for a bi-Maxwellian distribution. Therefore, along field lines as B increases, the pressure anisotropy decreases. As $(T_o/T_{||})$ decreases, not only the pressure anisotropy increases, but plasma beta also increases. Figure 4 shows the constant ψ contours for $(T_o/T_{||}) = 2$, which corresponds to a pressure anisotropy $P_\perp/P_{||} = 2$ on equator. The solid lines correspond to the equilibrium magnetic flux surfaces, and the dotted lines represent the dipole magnetic flux surfaces. In the high field region where beta is low, the solid curves and the dotted lines coincide for the same flux values. In the low field region the flux surfaces are much more drastically shifted outward than the isoptropic case due to higher values of parallel and perpendicular betas.

Figures 5(a) and 5(b) show the constant $P_{||}$ and $P_\perp$ contours for $(T_o/T_{||}) = 2$, respectively. The dotted lines correspond to the equilibrium constant ψ surfaces. Note that the surfaces of constant pressure are quite significantly shifted in relation to the surfaces of constant ψ in low field region. The $P_\perp$ contours are found to be more displaced than the $P_{||}$ surfaces. This is the result of the weak dependence of the pressure on ψ and the ensuing dominant dependence on B near the equator. Along field lines as B becomes large near the earth, the pressure contours coincide with the constant ψ surfaces. Near the equator, where B is smaller, the parallel and perpendicular pressures are enhanced to provide an outward shift of the constant pressure surfaces for region with $(\partial P/\partial\psi) < 0$. These behaviors can also be understood from a single particle point of view by employing the adiabatic invariance of the magnetic moment, $\mu = v_\perp^2/2B$ and the total energy $\varepsilon =$

$v^2/2$ conservation. Since a trapped particle has relatively lower $v_\perp$ and higher $v_\parallel$ in low field region than in high field region, the parallel pressure is enhanced in low field region accordingly to provide an outward shift of the constant parallel pressure surfaces. For a given energy these particles with $B_o/B(\chi) < \mu B_o/\varepsilon < 1$ are trapped in low field region where $B < B(\chi)$ and do not contribute to pressure in high field region where $B > B(\chi)$. The deeply trapped particles in the low field mirror regions have larger perpendicular velocity than parallel velocity and will enhance the perpendicular pressure even more than the parallel pressure. With the same argument we can understand that in region with $(\partial P/\partial\psi) > 0$ (small R region) the constant pressure contours shift inward with respect to the constant magnetic flux surfaces as shown in Figs. 5(a) and 5(b).

The constant magnetic field (Mod-B) contours are shown in Figure 6, where the dotted lines correspond to the equilibrium constant ψ surfaces. Note that the surfaces of constant B are quite significantly deformed in high beta region near the equator due to the diamagnetic effect. Since the second term of Eq. (2.12) indicates that the toroidal ring current depends on the gradient of the magnetic field for anisotropic plasma, the deformation of the magnetic field will greatly modify the ring current pattern. Figures 7(a) and 7(b) show the the toroidal ring current contours for $(T_o/T_\parallel) = 3$ and 2, respectively; along the magnetic field lines the westward ring current can be peak away from the equator. The dotted lines correspond to the equilibrium constant ψ surfaces. Because the pressure anisotropy will contribute to a eastward current, the eastward current region expands outward around the equatorial plane, and the westward current becomes peak away from the equator. As beta or pressure anisotropy increase, the westward current contours become more indented bean shapes and eventually develop local peak away from the equator as shown in Fig. 7(b). Figure 8 shows the ring current versus χ along field lines for four flux surfaces for the $(T_o/T_\parallel) = 2$ case, where χ varies from 0 to π and corresponds to an equal arc length coordinate along field lines from the southern hemisphere to the northern hemisphere. These four flux surfaces cross the equator at (a) $R = 2.1R_E$, (b) $R = 4.7R_E$, (c) $R = 8.0R_E$, and (d) $R = 9.9R_E$, respectively. As $(T_o/T_\parallel)$ increases, these features related to pressure anisotropy are less pronounced. Since the plasma pressure is almost always aniostropic and plasma beta is quite high in the magnetosphere, the results suggest that, against common belief, the ring current can be peaked away from the equator.

The radial variations of the perpendicular plasma pressure $P_\perp$, the perpendicular plasma beta $\beta_\perp = 2P_\perp/B^2$, the toroidal ring current J_ϕ, and the percentage difference between the self-consistent magnetic field and dipole field $(B-B_D)/B_D$ in the equatorial plane are shown for the $(T_o/T_\parallel) = 2$ case in Figures 9(a)-(d), respectively. The parallel pressure has same profile as the perpendicular pressure. Note that the maxima of $P_\perp$ and $\beta_\perp$ are located at different radial locations

as shown in Figures 9(a) and 9(b). The peak $P_\perp$ is located at $R \approx 3.5R_E$, and the maximum $\beta_\perp$ is about 1.3 and is located at $R \approx 7R_E$. Figure 9(c) shows that the westward current is peaked at $R \approx 8R_E$, and the eastward current is peaked at $R \approx 2.5R_E$. The deformation of the magnetic field due to the ring current plasma pressure is shown in Figure 9(d); the depression of magnetic field is dominant near the peak pressure gradient, $(\partial P_\perp/\partial\psi)$, location. The deformation of the magnetic field depends on the pressure profile and the boundary condition. For this case the magnetic field is reduced for $R < 7R_E$ and enhanced for $R > 7R_E$.

4.3 Effect of Outer Boundary Condition

The inner boundary flux surface is usually only slightly changed even during geomagnetic storm times with a worldwide depression of the magnetic field at the earth's surface, and we set $B_I = 0$ without loss of generality. The outer boundary flux surface has more significant effect on the magnetospheric equilibrium, and its effect is examined by varying B_S. For negative values of B_S the outer flux boundary resembles a dayside compressed flux surface due to solar wind pressure. For positive B_S the outer flux boundary resembles a tail-like flux surface. The fixed parameter is $P_o = 0.5$.

First, we choose $B_S = -0.04$, and $(T_\perp/T_\parallel) = 2.2$ to simulate a dayside magnetosphere with a compressed boundary flux surface. Figure 10 shows the constant ψ contours with the solid lines corresponding to the equilibrium solution and the dotted lines representing the dipole magnetic flux surfaces. Similar to those shown in Figure 4, the solid curves and the dotted lines coincide for the same flux values in the high field region where plasma beta is low. In the low field region the flux surfaces are much more drastically shifted outward than those shown in Figure 4 due to the outer boundary effect. Near the boundary the field lines exhibit relatively angular corners away from equator, but the field line curvature is drastically reduced near the equator. The surfaces of constant pressure are quite significantly shifted in relation to the surfaces of constant ψ in low field region; the $P_\perp$ contours are more drastically displaced than the $P_\parallel$ surfaces, similar to the case with $B_S = 0$ shown in Figure 5. In Figure 11, the solid lines are constant magnetic field contours, and the dotted lines correspond to the equilibrium constant ψ surfaces. Similar to the case with $B_S = 0$ shown in Figure 6, the constant B contours are quite significantly deformed in high beta region around the equator due to the diamagnetic effect for $R < 7R_E$. But, for $R > 7R_E$ the magnetic field is very significantly enhanced. For $R > 8.5R_E$ the magnetic field increases with R. Near $R \approx 8R_E$ the magnetic field develops a sharp gradient which will give a significant contribution to pressure anisotropy current. Because of the development of sharp magnetic field gradient the computation

becomes increasingly difficult and more grid points must be employed. As $(T_o/T_{\|}) \rightarrow 2$, the magnetic field gradient becomes so sharp that the computation does not converge even when 150 grid points along the field line and 100 flux surfaces are employed. Figure 12 shows similar toroidal ring current contours as shown in Figure 7(b), but the westward ring current contours becomes more drastically changed for $R > 7R_E$. The dotted lines correspond to the equilibrium constant ψ surfaces. Figures 13(a)-(d) show the radial variations of the perpendicular plasma pressure $P_\perp$, the perpendicular plasma beta $\beta_\perp$, the toroidal ring current J_ϕ, and the percentage difference between the self-consistent magnetic field and dipole field $(B-B_D)/B_D$ in the equatorial plane, respectively. Note that the $\beta_\perp$ value shown in Figure 13(b) is about the sane as the $B_S = 0$ case shown in Figure 9(b). Figure 13(c) shows that the westward current is peaked at $R \approx 8.2R_E$, and the eastward current is peaked at $R \approx 2.5R_E$. The deformation of the magnetic field from dipole field shown in Figure 13(d) is roughly a factor of 1.5 larger than the $B_S = 0$ case shown in Figure 9(d).

To simulate the effect of a tail-like boundary flux surface on the magnetospheric equilibrium we set $B_S = 0.2$, and $(T_o/T_{\|}) = 2$. Figure 14 shows the constant ψ contours with the solid lines corresponding to the equilibrium solution and the dotted lines representing the dipole magnetic flux surfaces. The solid curves and the dotted lines coincide for the same flux values in the high field region where plasma beta is low. In the low field region the flux surfaces shift inward due to the tail-like outer boundary. The finite beta effect causes the surfaces of constant pressure to significantly shift outward in relation to the surfaces of constant ψ in low field region, and the $P_\perp$ contours are found to be more displaced than the $P_{\|}$ surfaces. In Figure 15 the solid lines are constant magnetic field contours, and the dotted lines correspond to the equilibrium constant ψ surfaces. Similar to the case with $B_S = 0$ shown in Figure 6, the surfaces of constant B are quite significantly deformed in high beta region near the equator. Figure 16 shows the toroidal ri current contours with the westward ring current peaking away from the equator. The dotted lines correspond to the equilibrium constant ψ surfaces. Figures 17(a)-(d) show the radial variations of the perpendicular plasma pressure $P_\perp$, the perpendicular plasma beta $\beta_\perp$, the toroidal ring current J_ϕ, and the percentage difference between the self-consistent magnetic field and dipole field $(B-B_D)/B_D$ in the equatorial plane, respectively. Note that the $\beta_\perp$ value shown in Figure 17(b) is significantly reduced in comparison with the $B_S = 0$ case shown in Figure 9(b) due to enhanced magnetic field. Figure 17(c) shows that the westward current is peaked at $R \approx 6R_E$, and the eastward current is peaked at $R \approx 2.5R_E$. Contrary to previous cases Figure 17(d) shows that the magnetic field is enhanced relative to the dipole field for $R < 8R_E$ and is reduced for $R > 8R_E$.

5. Summary and Discussion

Self-consistent axisymmetric magnetospheric equilibrium with anisotropic pressure is obtained by employing an iterative metric method for solving the inverse equilibrium equation. The iterative metric method uses finite differences in an optimal flux coordinate system which is iterated for simultaneously with the equilibrium solution until one coordinate coincides with the magnetic surfaces. The method automatically accumulates grid points in regions of steep gradients, thus yielding accurate solutions of high β magnetospheric equilibria. A method of determining plasma parallel and perpendicular pressures from either analytic particle distribution or particle distribution measured along the satellite's path by using invariance of the magnetic moment to determine its value at each point along field lines is also presented. The numerical results of axisymmetric magnetospheric equilibrium including the effects of finite beta, pressure anisotropy, and boundary conditions are studied for a bi-Maxwellian particle distribution for simplicity. For the isotropic pressure case, the finite beta effect produces outward expansion of the constant magnetic flux surfaces in relation to the dipole field lines, and along the magnetic field the toroidal ring current is maximum at the magnetic equator. The effect of pressure anisotropy is found to further expand the flux surfaces outward. The magnetic field is deformed and is reduced around the peak perpendicular pressure gradient location. Along the magnetic field lines the westward ring current is peak away from the equator due to an eastward current contribution resulting from pressure anisotropy. As pressure anisotropy increases, the peak westward current can become more singular. The results suggest that, against common belief, along the field lines the westward ring current can be peaked away from the equator in the magnetosphere, where the plasma pressure is almost always aniostropic and the plasma beta is quite high. The effects of pressure anisotropy on the pressure contours can be understood by noting that the particles are trapped in the lower magnetic field region. The conservation of particle energy and the adiabatic invariance of the magnetic moment dictate that trapped particles will have relatively larger perpendicular velocity and smaller parallel velocity in high magnetic field regions than in low field regions, the parallel pressure is enhanced in low field region accordingly to provide an outward shift of the constant parallel pressure surfaces. The deeply trapped particles in the low field mirror regions have larger perpendicular velocity than parallel velocity and will enhance the perpendicular pressure even more than the parallel pressure. The outer boundary flux surface has significant effect on the magnetospheric equilibrium. For outer flux boundary resembling a dayside compressed flux surface due to solar wind pressure, these finite beta and pressure anisotropy effects described above are greatly enhanced. For outer flux boundary resembling a tail-like flux surface, the deformation of the magnetic field is quite different.

The results presented in the paper agree very well qualitatively with satellite observations [Lui et al., 1987; Williams, 1983]. In order to provide a more conclusive test of the magnetospheric equilibrium calculations with satellite observations, a detail information of ring current particle distribution and better boundary conditions may be required. For the information of particle distribution, issues related to the sources and composition of ring current particles as well as energization and injection processes associated with the storm time ring current formation are yet to be resolved. Although significant progress has been made in the satellite observational data of ring current particle distribution, more complete information is required to give full energy and pitch angle range and wider radial and azimuthal spatial coverage. Lower charge states of Oxygen ions, presumably injected from the ionosphere may have energy content as much as 30% of the total ring current energy, must also be included. Exploration of new observational data of ring current particle distributions must be made. For the boundary conditions, we shall explore a more complicated form of ψ_{max} than that defined by Eq.(4.1) and also employ empirical shapes from magnetic field models.

The whole magnetospheric equilibrium is not axisymmetric and the problem requires a full three-dimensional treatment with complex topology. The two-dimensional inverse method code presented in this paper can be extended to three-dimensional calculations without conceptual difficulty. A natural extension is to study a three-dimensional equilibrium without toroidal magnetic field by specifying fixed boundary magnetic flux surfaces. The next step is to relax the constraint of zero toroidal magnetic field. Eventually, our goal is to determine the outer magnetic flux surface (magnetopause) self-consistently by considering all the major magnetospheric current systems outside the magnetopause [Olson and Pfitzer, 1977]. The shape of the magnetopause will be determined iteratively as part of the equilibrium solution by a pressure balance between the magnetic field and a steady solar wind with the requirement that the normal component of the magnetic field vanish at the boundary [Mead and Beard, 1964].

Acknowledgments

This work is supported by the NSF Grant No. ATM-8911638 and DoE Contract No. DE-AC02-76-CHO3073. The author would like to thank Drs. A. T. Y. Lui, D. Monticello, and G.-H. Voigt for useful discussions.

References

Akasofu, S. I., and S. Chapman, The ring current, geomagnetic disturbance, and the Van Allen radiation belts, J. Geophys. Res., 66, 1321, 1961.

Berko, F. W., L. J. Cahill, Jr., and T. A. Fritz, Proton as the prime contributors to storm time ring current, J. Geophys. Res., 86, 3549, 1975.

Cheng, C. Z., and C. S. Lin, Eigenmode analysis of compressional Alfvén waves in the magnetosphere, Geophys. Res. Lett., 14, 884, 1987.

Cheng, C. Z., Computation of the magnetospheric equilibrium, EOS, 71, 615, 1990.

DeLucia, J., S. C. Jardin, and A. M. M. Todd, An iterative metric method for solving the inverse tokamak equilibrium problem, J. Comp. Phys., 37, 183, 1980.

Grad, H., in Magneto-Fluid and Plasma Dynamics, Symposia in Applied Mathematics (Am. Math. Soc.), 18, 162, 1967.

Heinemann, H., Representations of currents and magnetic fields in anisotropic magnetohydrostatic plasma, J. Geophys. Res., 95, 7789, 1990.

Hoffman, R. A., and P. A. Bracken, Higher-order ring currents and particle energy storage in the magnetosphere, J. Geophys. Res., 72, 6039, 1967.

Ip, A. K., G.-H. Voigt, Plasma-dominated magnetic field configurations for the magnetosphere of Uranus, J. Geophys. Res., 90, 6287, 1985.

Longmire, C. L., Elementary plasma physics, John Wiley, New York, 1963.

Lui, A. T. Y., R. W. McEntire, and S. M. Krimigis, Evolution of the ring current during two geomagnetic storms, J. Geophys. Res., 92, 4759, 1987.

Mead, G. D., and D. B. Beard, Shape of the geomagnetic field solar wind boundary, J. Geophys. Res., 69, 1169, 1964.

Olson, W. P., and K. A. Pfitzer, Magnetic field modeling, McDonnell Douglas Astronautics Company Annual Scientific Report to AFOSR, January 1977.

Roache, P. J., Computational Fluid Dynamics, Hermosa Publishers, Albuquerque, N.M., Library of Congress Catalog Card Number 72-89970, p. 117, 1972.

Spence, H. E., M. G. Kivelson, and R. J. Walker, Magnetospheric plasma pressures in the midnight meridian: Observations from 2.5 to 35 R_E, J. Geophys. Res. 94, 5264, 1989.

Toffoletto, F. R., and T. W. Hill, Quantitative model of magnetic coupling between solar wind and magnetosphere, in Proceedings of the Chapman Conference on Solar Wind-Magnetosphere Coupling, edited by Y. Kamide and J. Slavin, Terra/Reidel, Tokyo, 1986.

Voigt, G.-H., A mathematical magnetospheric field model with independent physical parameters, Planet. Space Sci., 29,1, 1981.

Voigt, G.-H.,T. W. Hill, and A. J. Dessler, The magnetosphere of Uranus: Plasma source, convection and field configuration, Astrophys. J., 266, 390, 1983.

Voigt, G.-H., Field line twist and field-aligned currents in an axisymmetric equilibrium magnetosphere, J. Geophys. Res., 91, 10995, 1986a.

Voigt, G.-H., Magnetospheric equilibrium configurations and slow adiabatic convection, in Proceedings of the Chapman Conference on Solar Wind-Magnetosphere Coupling, edited by Y. Kamide and J. Slavin, p. 233, Terra/Reidel, Tokyo, 1986b.

Whipple, E., R. Puetter, and M. Rosenberg, A two-dimensional, time-dependent, near-earth magnetotail, COSPAR Journal "Advances in Space Research", 1990.

Williams, D. J., The earth's ring current: Causes, generation, and decay, in Progress in Solar-Terrestrial Physics, edited by J. G. Roederer, p. 223, D. Reidel, Hingham, Mass., 1983.

Zavriyev, A., and A. Hasegawa, The equilibrium dayside magnetosphere, J. Geophys Res., 94, 10039, 1989.

Figure Captions

Fig. 1 The constant ψ contours for isotropic pressure with $P_o = 0.5$, $B_I = B_S = 0$, $(T_o/T_{||})=10^4$. The solid lines correspond to the equilibrium solution, and the dotted lines represent the dipole magnetic flux surfaces.

Fig. 2 The toroidal ring current contours with same parameters as in Fig. 1. Along the magnetic field lines the ring current is peak at the equator. The dotted lines correspond to the equilibrium constant ψ surfaces. The ring current is eastward at small R and is westward at large R.

Fig.3 The radial variations of (a) the plasma pressure P, (b) the plasma beta β, (c) the toroidal ring current J_ϕ, and (d) the percentage difference between the self-consistent magnetic field and dipole field $(B-B_D)/B_D$ in the equatorial plane with same parameters as in Fig. 1.

Fig.4 The constant ψ contours for $P_o = 0.5$, $B_I = B_S = 0$, and $(T_o/T_{||}) = 2$, which corresponds to a pressure anisotropy $P_\perp/P_{||} = 2$ at the equator. The solid lines correspond to the equilibrium solution, and the dotted lines represent the dipole magnetic flux surfaces.

Fig. 5 (a) The constant $P_{||}$ contours and (b) the constant $P_\perp$ contours with same parameters as in Fig. 4 . The dotted lines correspond to the equilibrium constant ψ surfaces.

Fig. 6 The constant magnetic field (Mod-B) contours with same parameters as in Fig. 4, where the dotted lines correspond to the equilibrium constant ψ surfaces.

Fig. 7 (a) The toroidal ring current contours with same parameters as in Fig. 4, but $(T_o/T_{||}) = 3$. The dotted lines correspond to the equilibrium constant ψ surfaces. The ring current is eastward at small R and is westward at large R. (b) The toroidal ring current contours with same parameters as in Fig. 4 with $(T_o/T_{||}) = 2$.

Fig. 8 The ring current versus χ along field lines for four different flux surfaces, where χ varies from 0 to π. These four flux surfaces cross the equator at (a) $R = 2.165R_E$, (b) $R = 4.74R_E$, (c) $R = 8.04R_E$, and (d) $R = 9.9R_E$, respectively. The parameters are same as in Fig. 4.

Fig.9 The radial variations of (a) the perpendicular plasma pressure $P_\perp$, (b) the perpendicular plasma beta $\beta_\perp$, (c) the toroidal ring current J_ϕ, and (d) the percentage difference between the self-consistent magnetic field and dipole field $(B-B_D)/B_D$ in the equatorial plane with same parameters as in Fig. 4.

Fig.10 The constant ψ contours for $P_o = 0.5$, $B_I = 0$, $(T_o/T_\parallel) = 2.2$, and $B_S = -0.04$. The pressure anisotropy $P_\perp/P_\parallel = 1.833$ at the equator. The outer boundary flux surface resembles a dayside compressed flux surface. The solid lines correspond to the equilibrium solution, and the dotted lines represent the dipole magnetic flux surfaces.

Fig. 11 The constant magnetic field (Mod-B) contours with same parameters as in Fig. 10, where the dotted lines correspond to the equilibrium constant ψ surfaces.

Fig. 12 The toroidal ring current contours with same parameters as in Fig. 10. The dotted lines correspond to the equilibrium constant ψ surfaces. The ring current is eastward at small R and is westward at large R.

Fig.13 The radial variations of (a) the perpendicular plasma pressure $P_\perp$, (b) the perpendicular plasma beta $\beta_\perp$, (c) the toroidal ring current J_ϕ, and (d) the percentage difference between the self-consistent magnetic field and dipole field $(B-B_D)/B_D$ in the equatorial plane with same parameters as in Fig. 10.

Fig.14 The constant ψ contours for $P_o = 0.5$, $B_I = 0$, $(T_o/T_\parallel) = 2$, and $B_S = 0.2$. The pressure anisotropy $P_\perp/P_\parallel = 2$ at the equator. The outer boundary flux surface resembles a tail-like flux surface. The solid lines correspond to the equilibrium solution, and the dotted lines represent the dipole magnetic flux surfaces.

Fig. 15 The constant magnetic field (Mod-B) contours with same parameters as in Fig. 14, where the dotted lines correspond to the equilibrium constant ψ surfaces.

Fig. 16 The toroidal ring current contours with same parameters as in Fig. 14. The dotted lines correspond to the equilibrium constant ψ surfaces. The ring current is eastward at small R and is westward at large R.

Fig.17 The radial variations of (a) the perpendicular plasma pressure $P_\perp$, (b) the perpendicular plasma beta $\beta_\perp$, (c) the toroidal ring current J_ϕ, and (d) the percentage difference between

the self-consistent magnetic field and dipole field $(B-B_D)/B_D$ in the equatorial plane with same parameters as in Fig. 14.

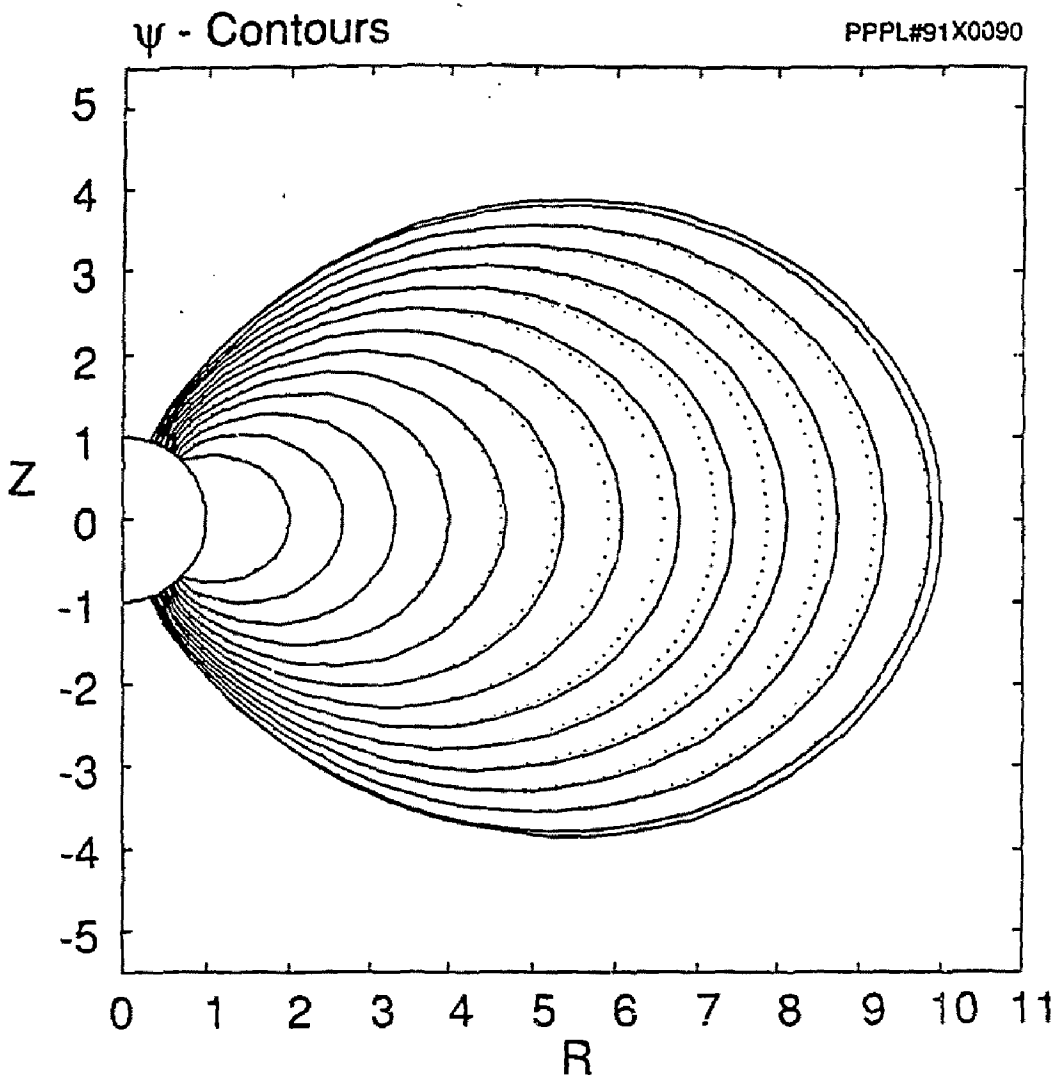

Fig. 1

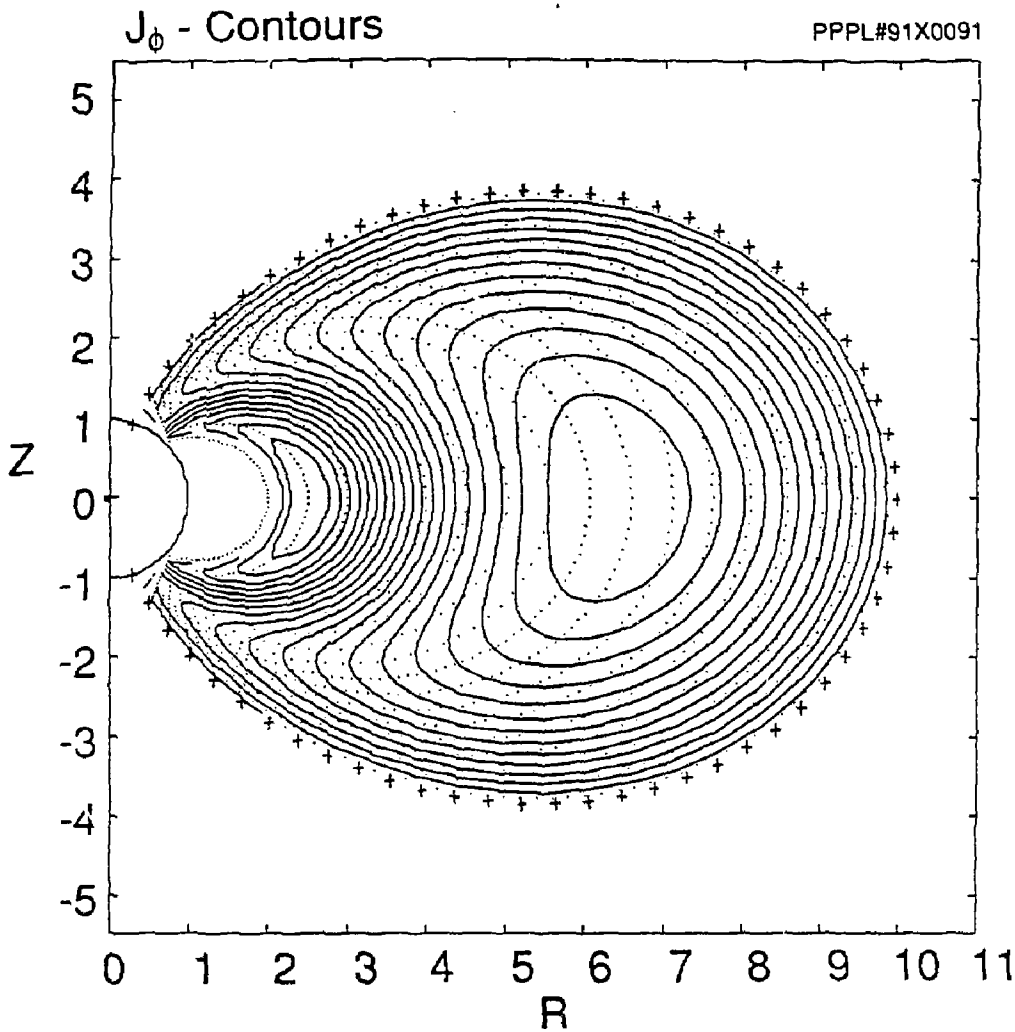
J_ϕ - Contours
PPPL#91X0091
Z
R
5
4
3
2
1
0
-1
-2
-3
-4
-5
0
1
2
3
4
5
6
7
8
9
10
11

Fig. 2

PPPL#91X0103

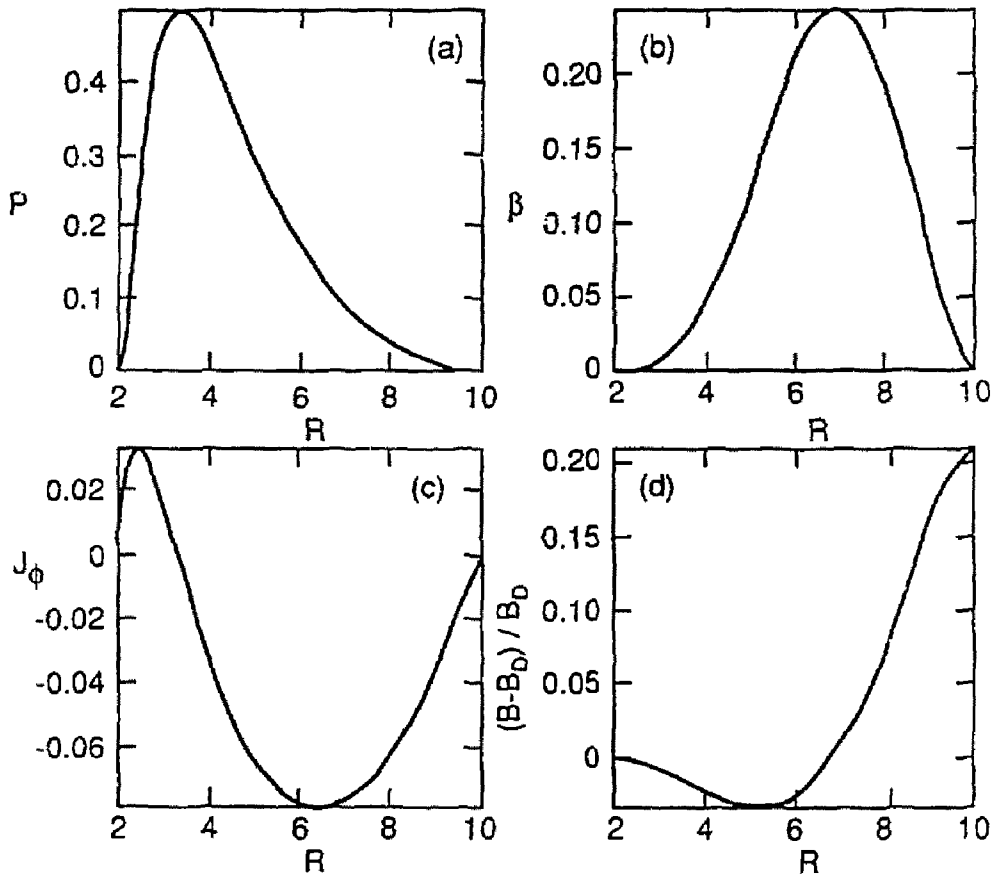

Fig. 3

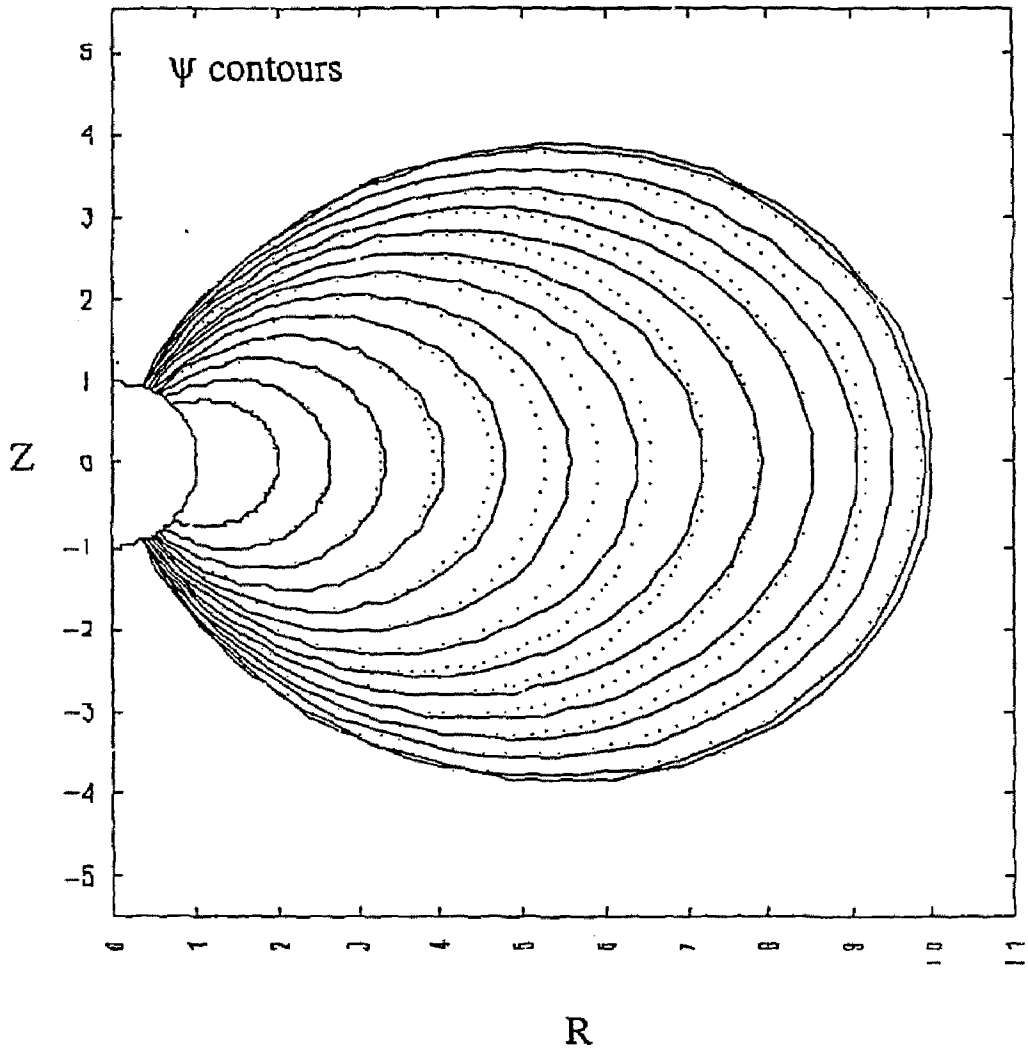

Fig. 4

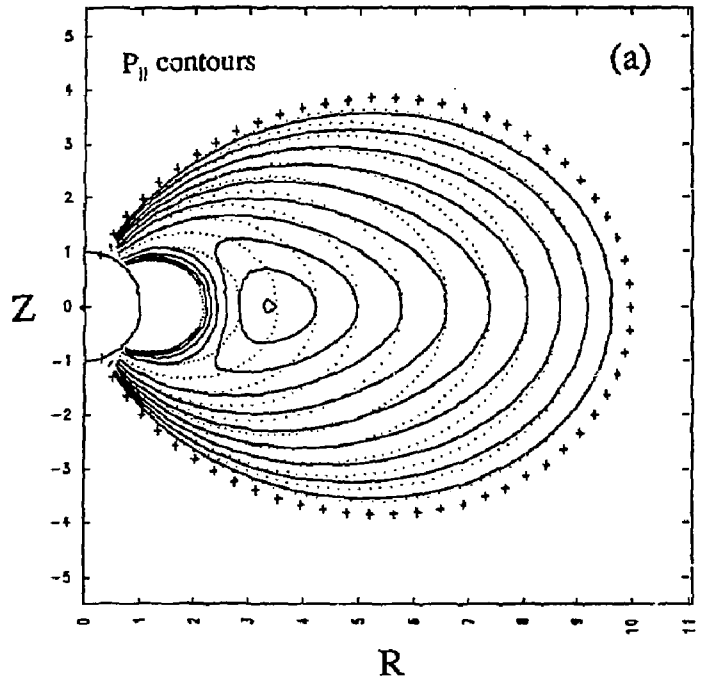

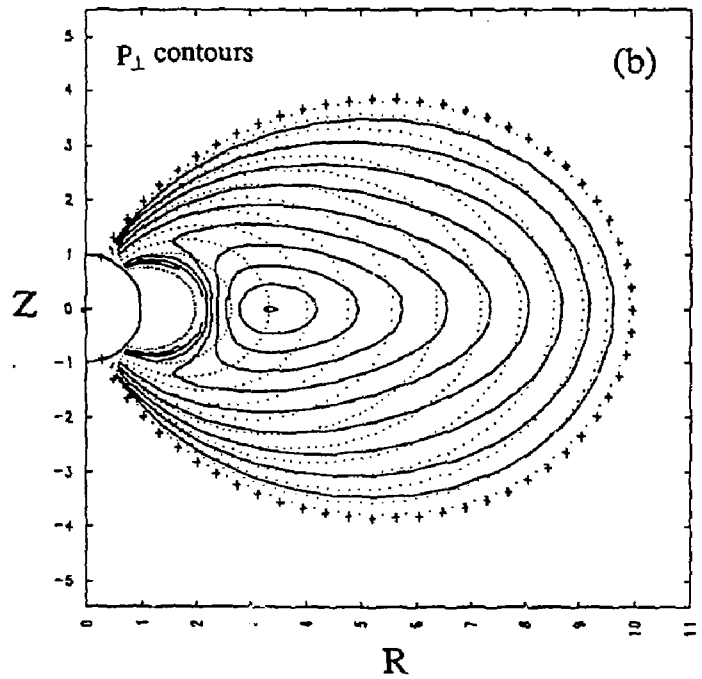

Fig. 5

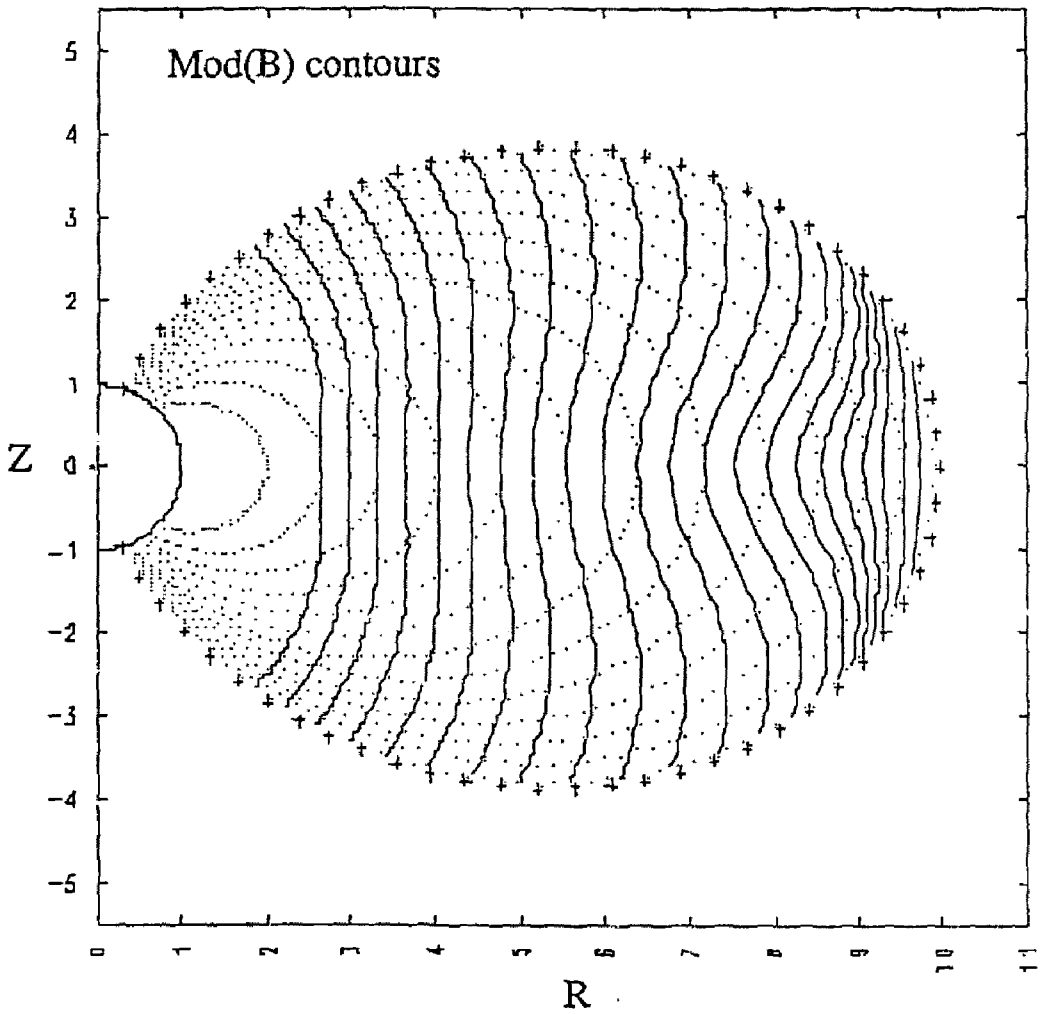

Fig. 6

J_ϕ contours

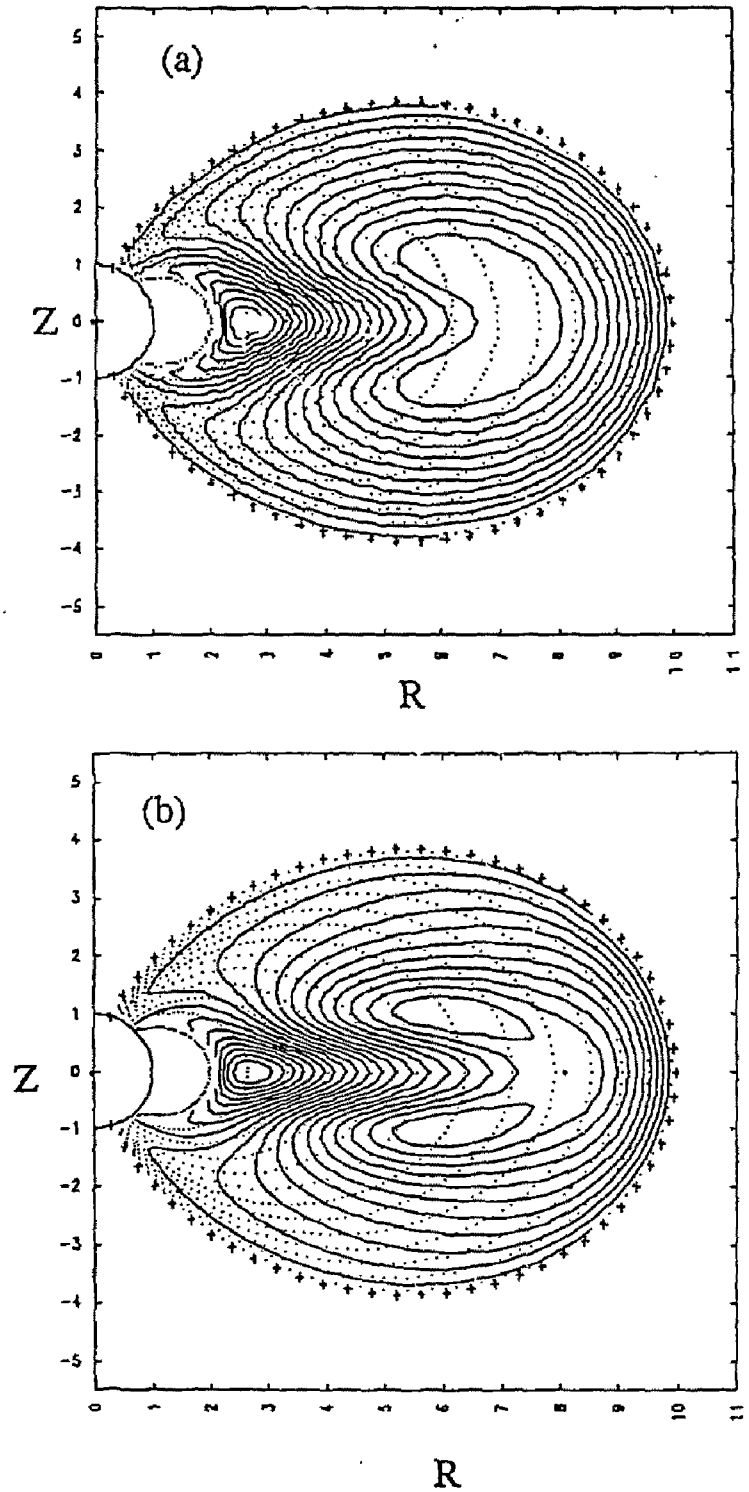

Fig. 7

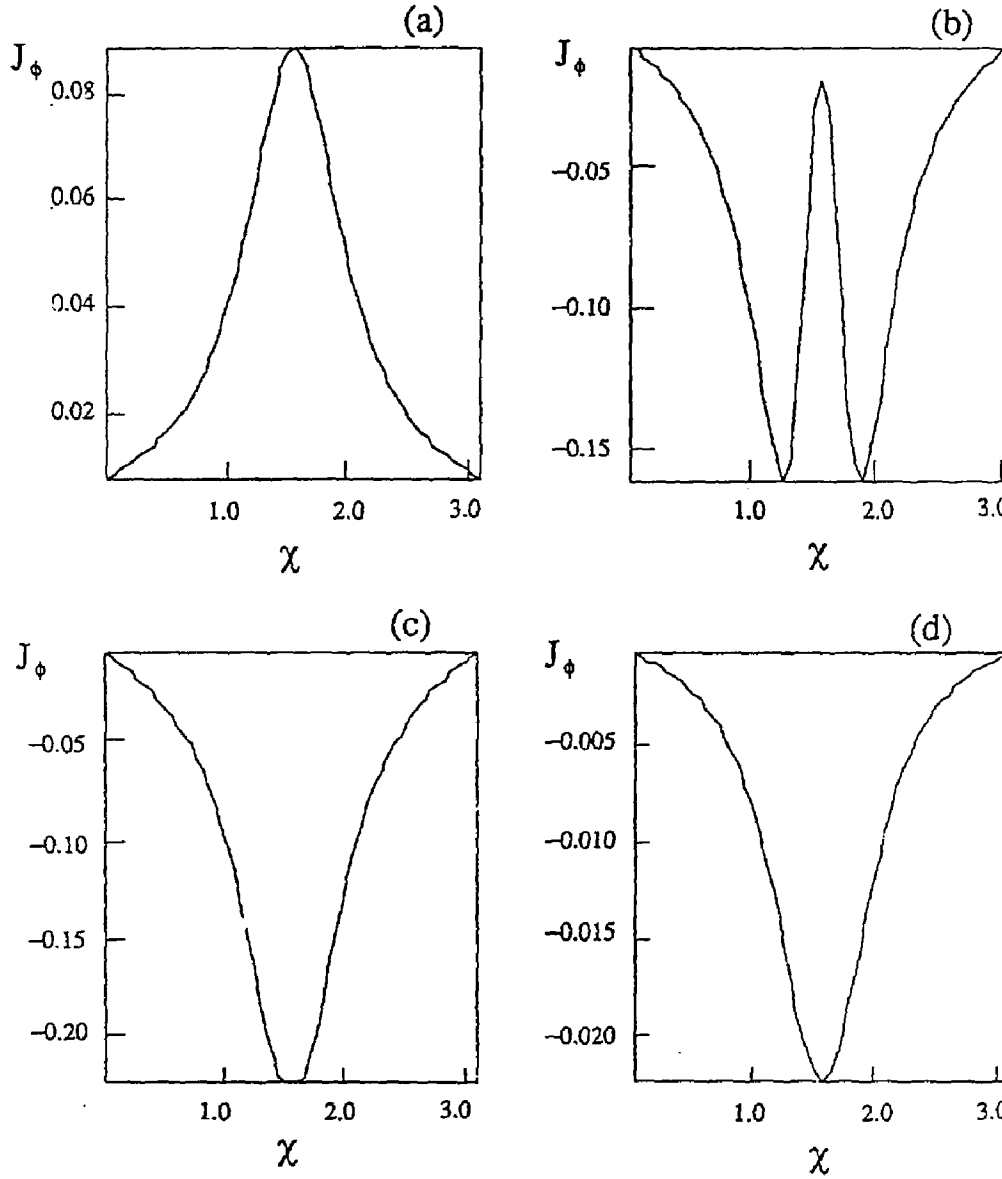
(a)
J_ϕ
0.08
0.06
0.04
0.02
1.0
2.0
3.0
χ
(b)
J_ϕ
−0.05
−0.10
−0.15
1.0
2.0
3.0
χ
(c)
J_ϕ
−0.05
−0.10
−0.15
−0.20
1.0
2.0
3.0
χ
(d)
J_ϕ
−0.005
−0.010
−0.015
−0.020
1.0
2.0
3.0
χ

Fig. 8

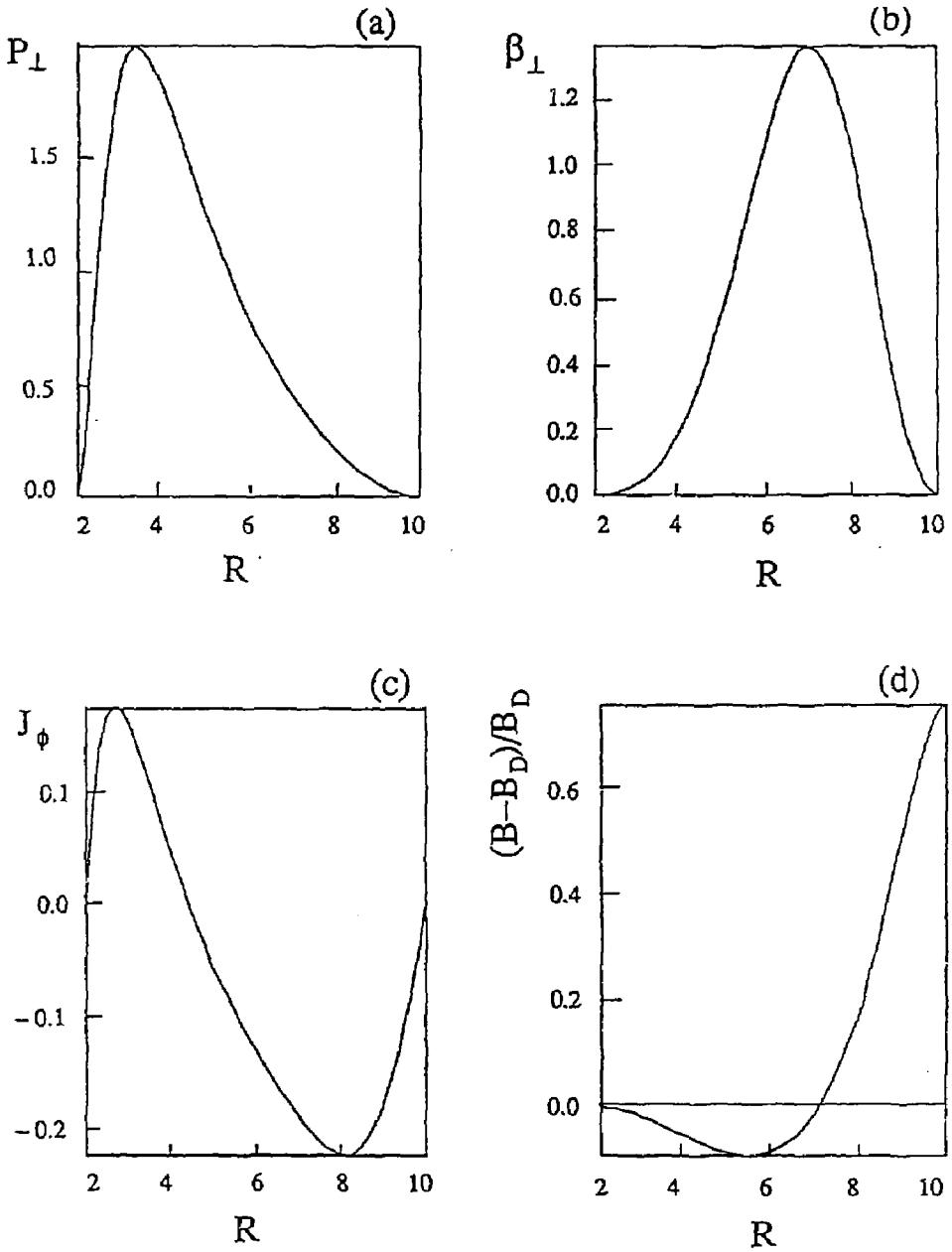
(a)
$P_\perp$
1.5
1.0
0.5
0.0
2
4
6
8
10
R
(b)
$\beta_\perp$
1.2
1.0
0.8
0.6
0.4
0.2
0.0
2
4
6
8
10
R
(c)
J_ϕ
0.1
0.0
−0.1
−0.2
2
4
6
8
10
R
(d)
$(B-B_D)/B_D$
0.6
0.4
0.2
0.0
2
4
6
8
10
R

Fig. 9

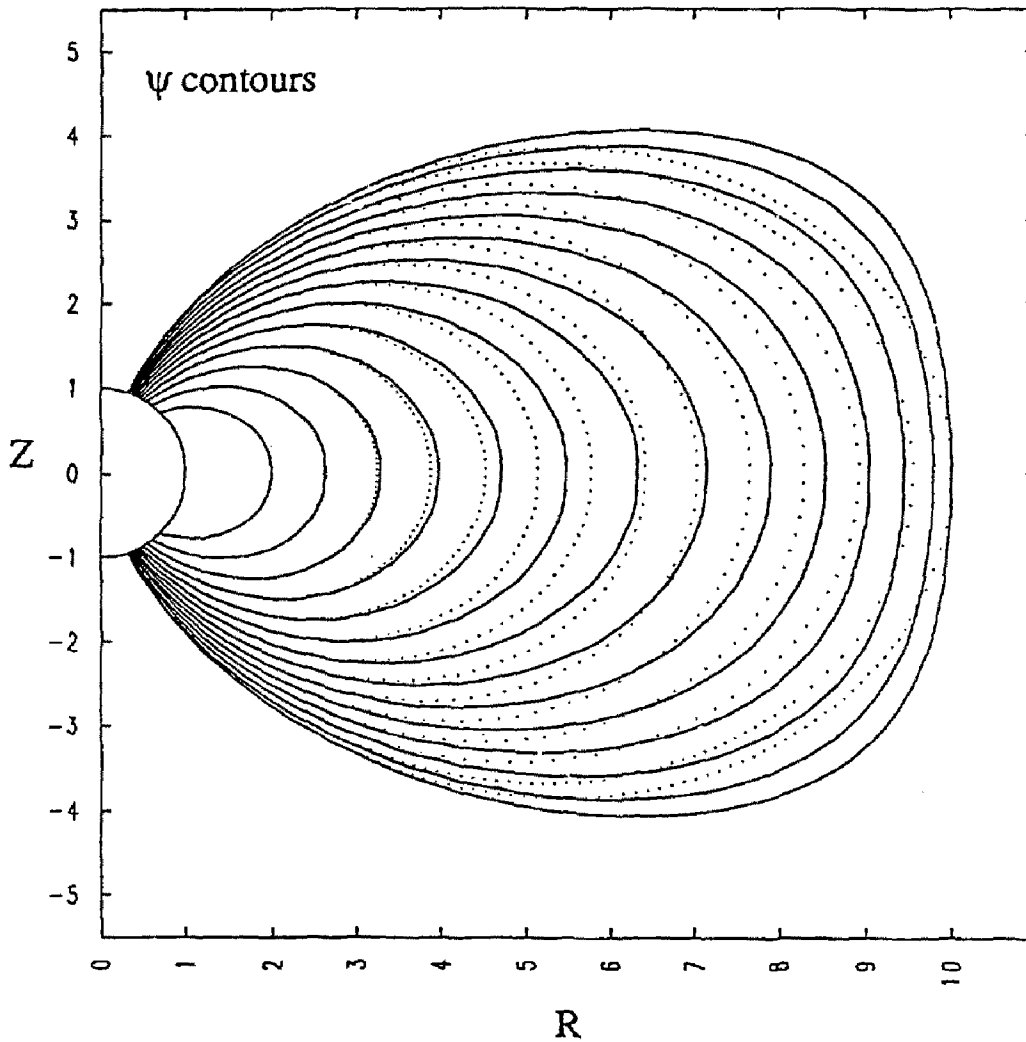

Fig. 10

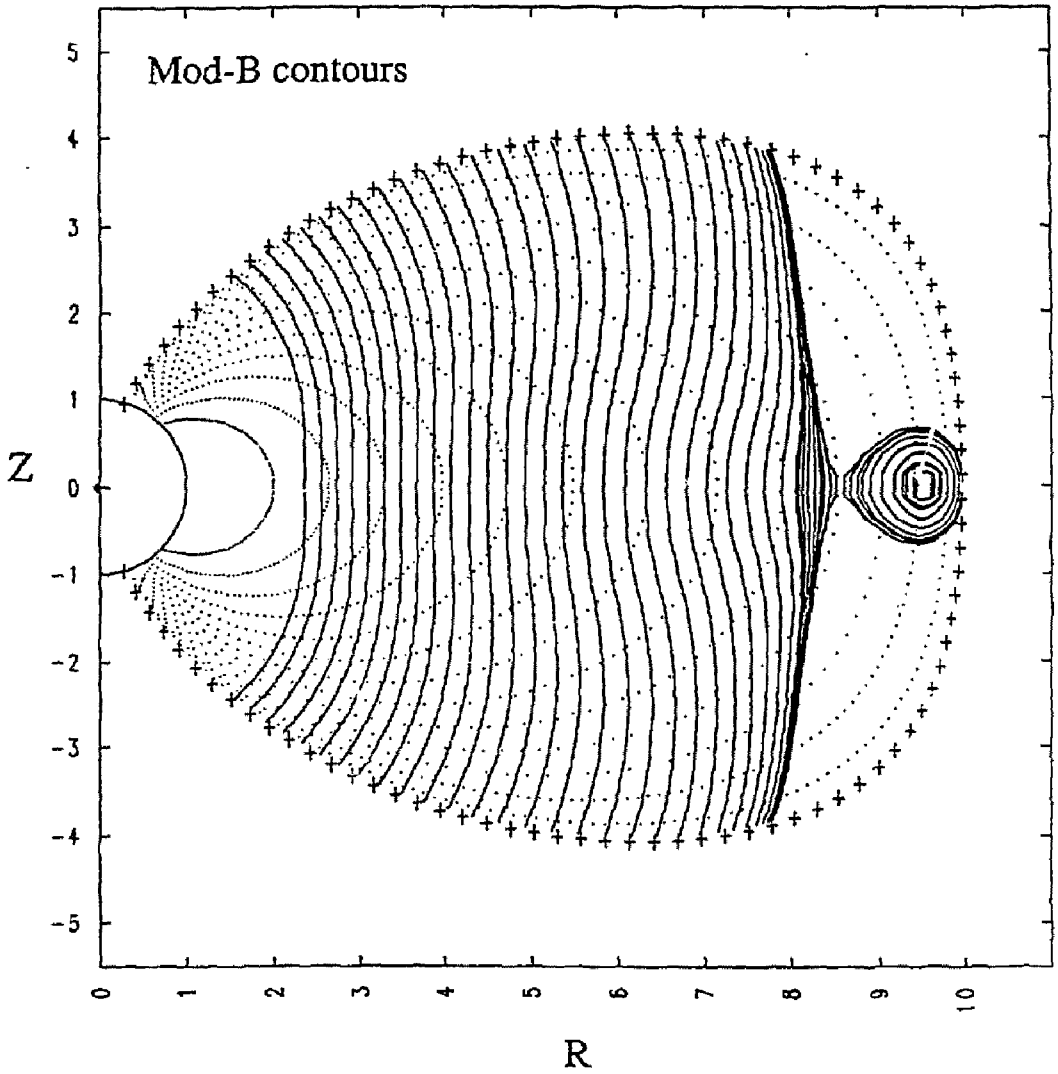

Fig. 11

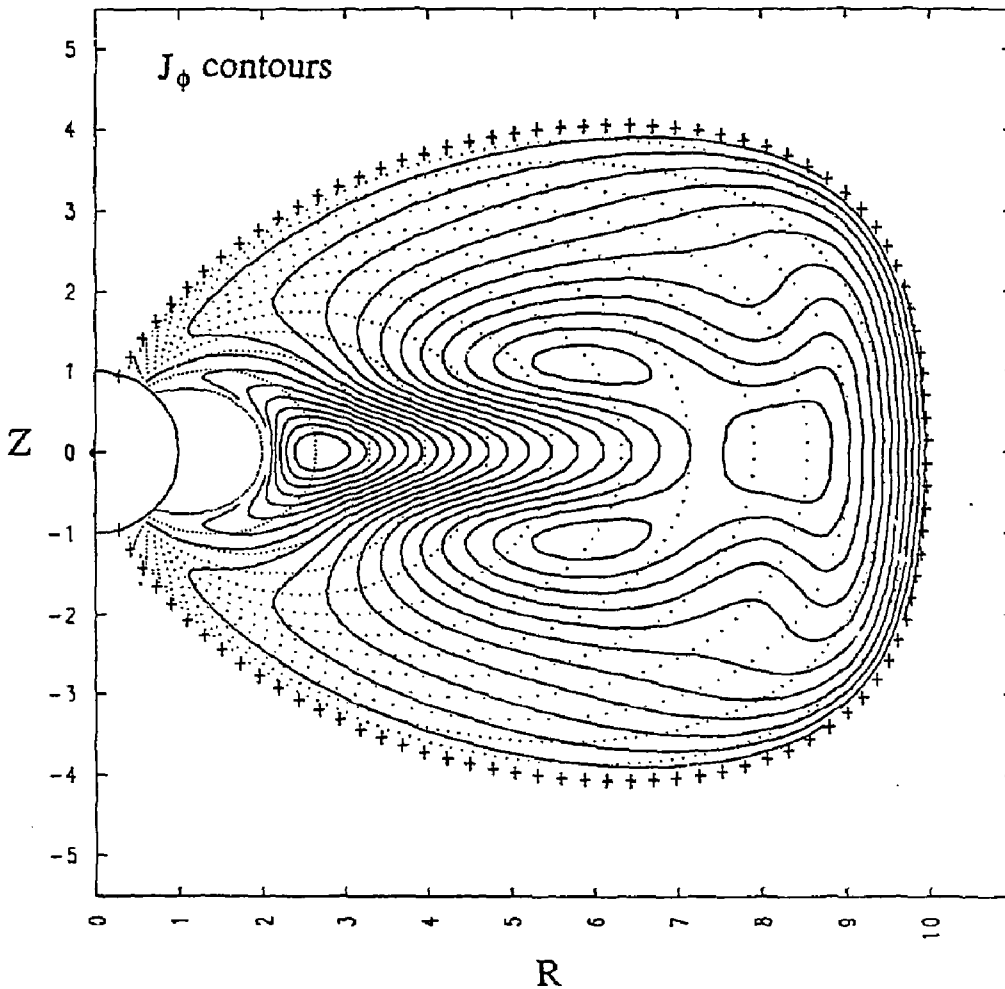

Fig. 12

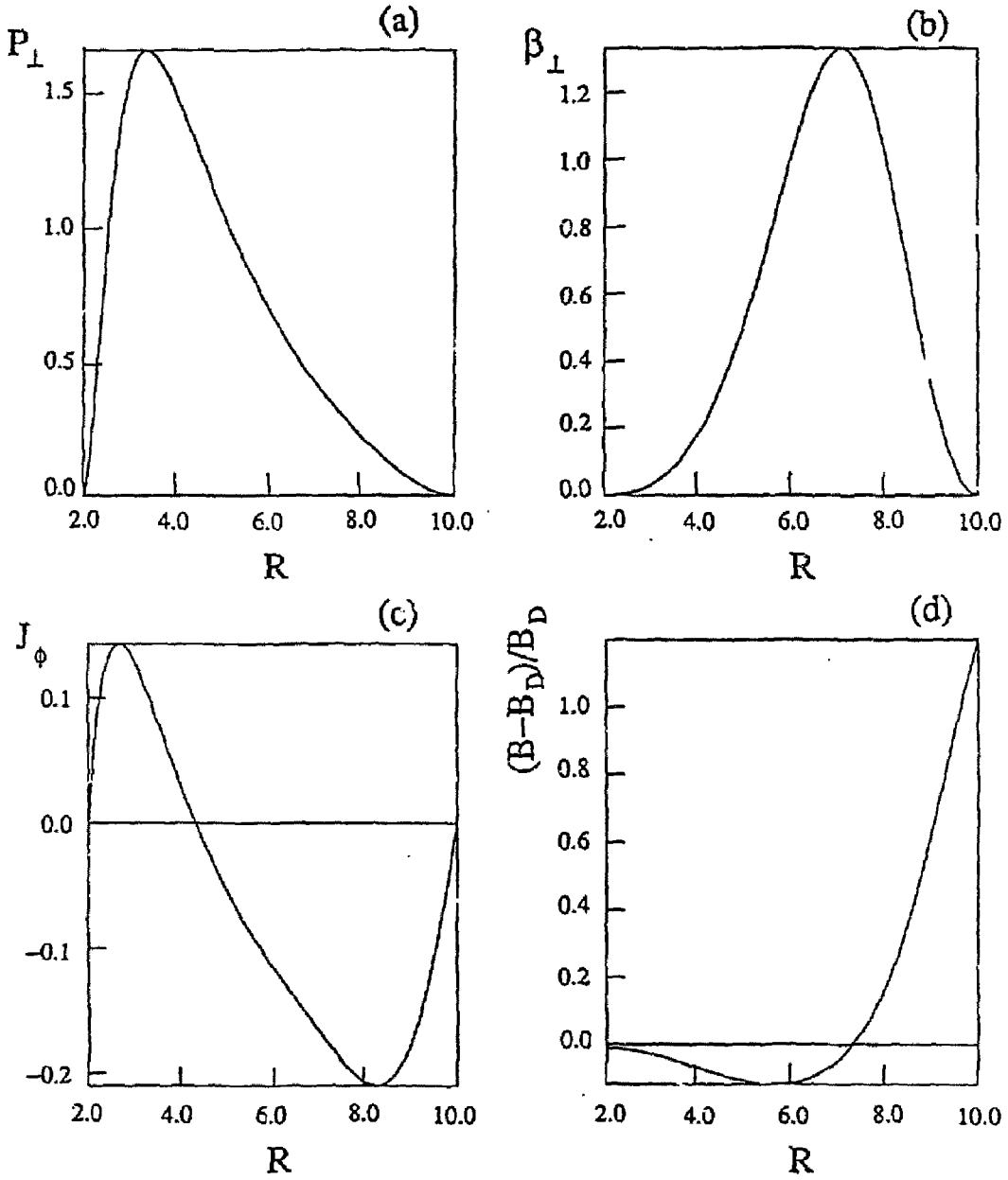
(a)
$P_\perp$
1.5
1.0
0.5
0.0
2.0
4.0
6.0
8.0
10.0
R
(b)
$\beta_\perp$
1.2
1.0
0.8
0.6
0.4
0.2
0.0
2.0
4.0
6.0
8.0
10.0
R
(c)
J_ϕ
0.1
0.0
−0.1
−0.2
2.0
4.0
6.0
8.0
10.0
R
(d)
$(B-B_D)/B_D$
1.0
0.8
0.6
0.4
0.2
0.0
2.0
4.0
6.0
8.0
10.0
R

Fig. 13

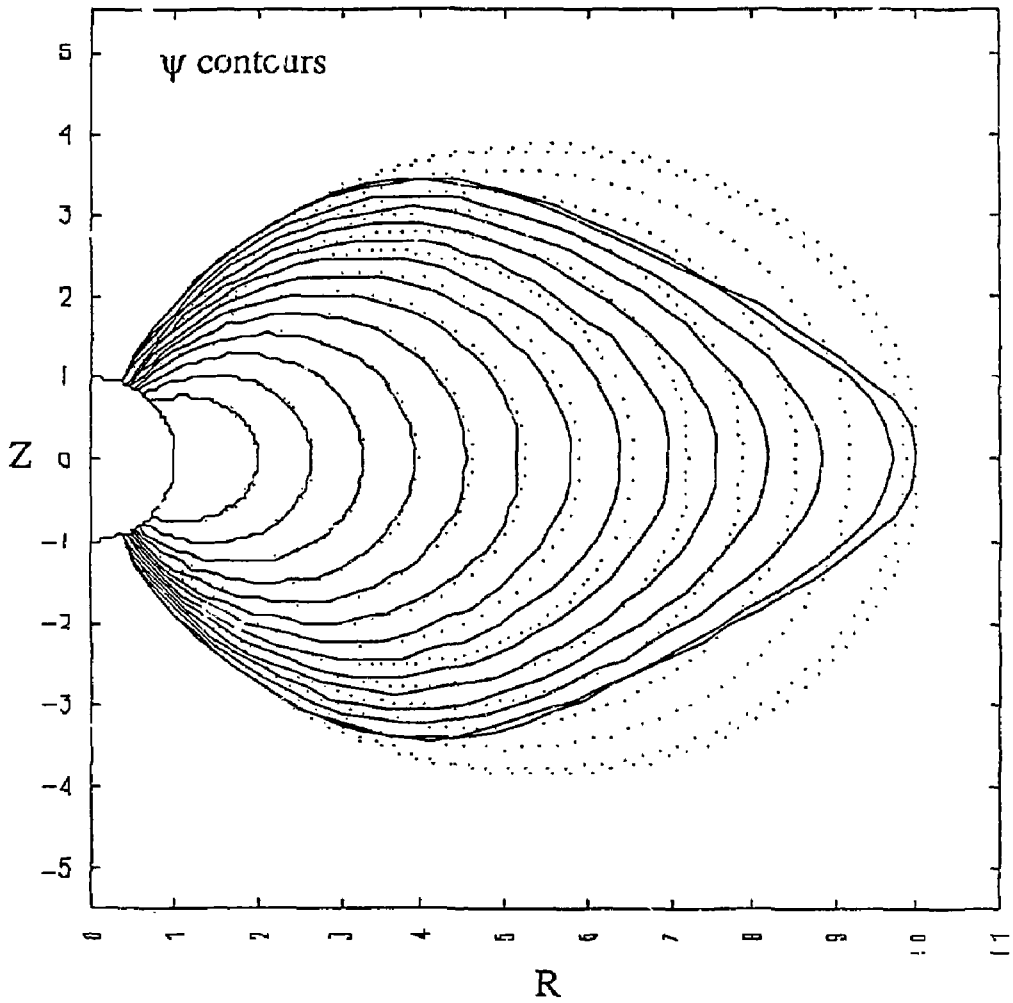

Fig. 14

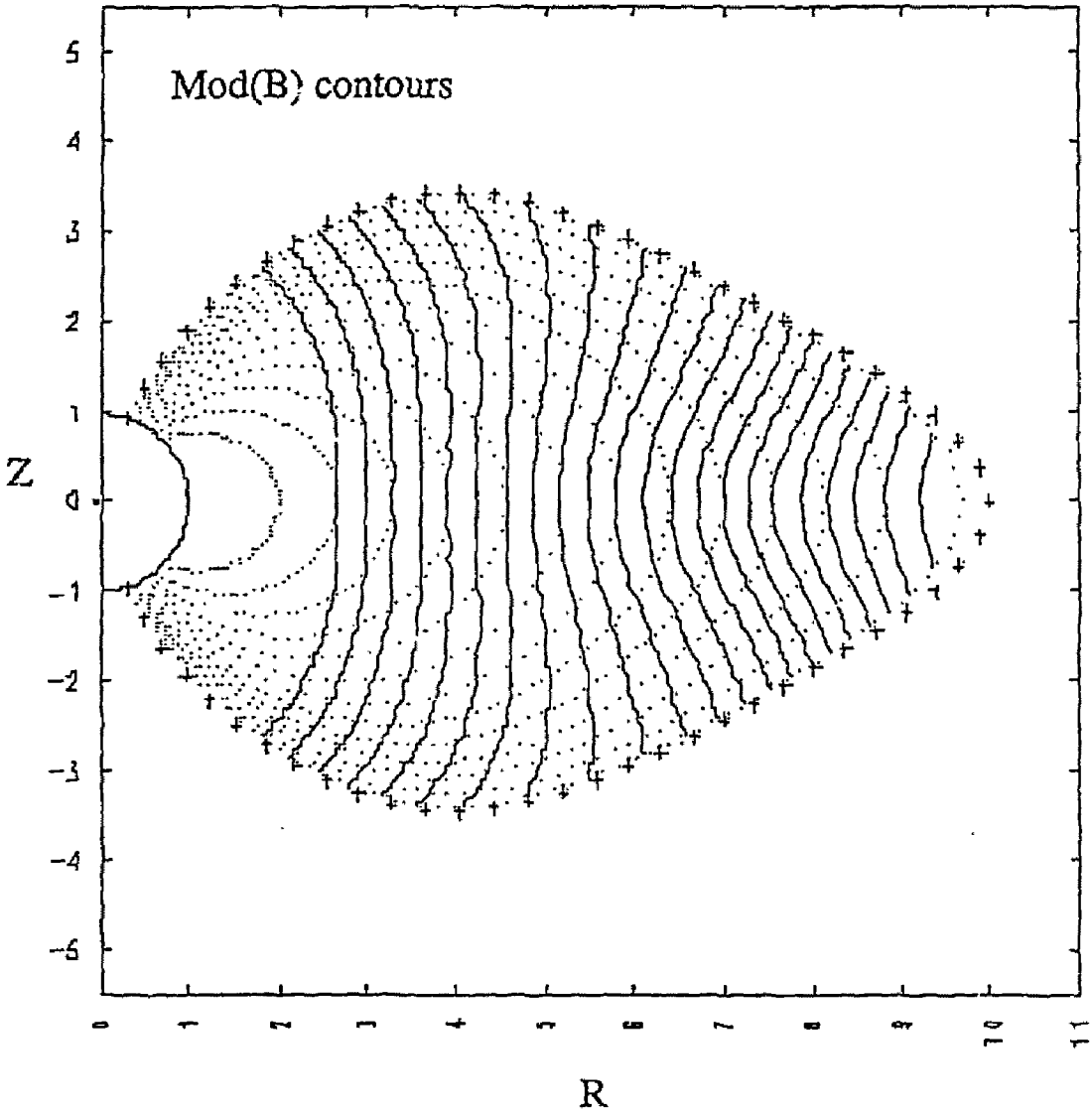

Fig. 15

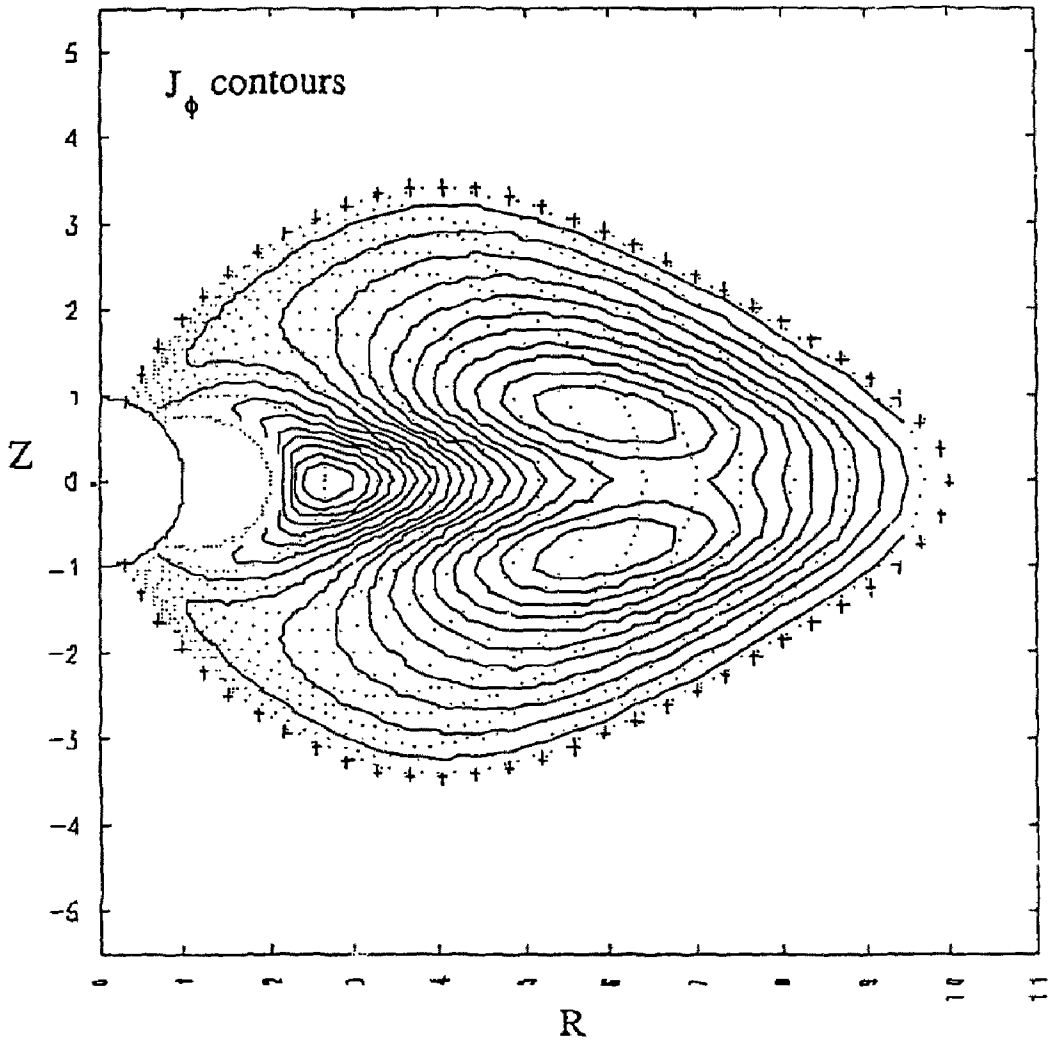

Fig. 16

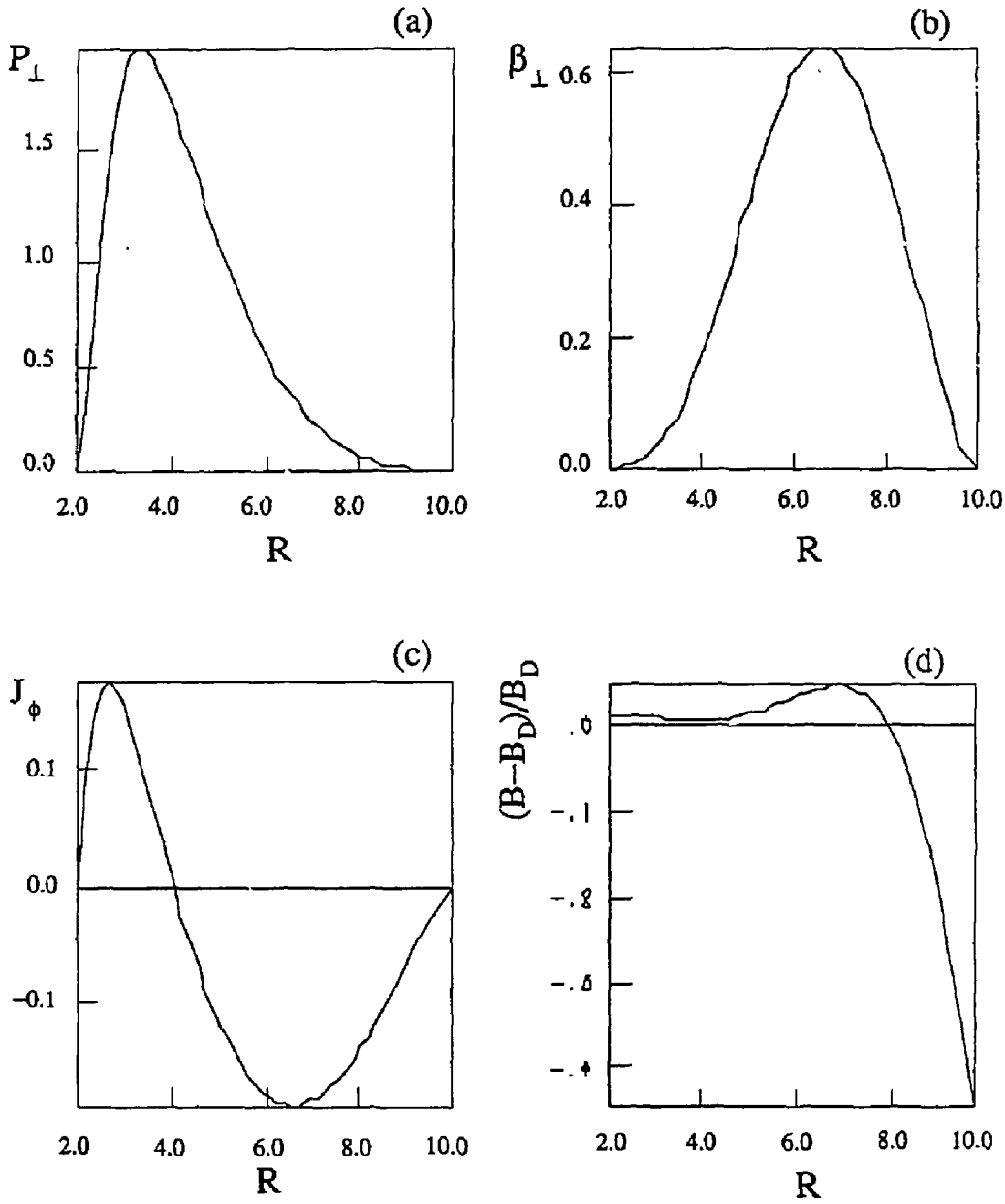
(a)
$P_\perp$
1.5
1.0
0.5
0.0
2.0
4.0
6.0
8.0
10.0
R
(b)
$\beta_\perp$
0.6
0.4
0.2
0.0
2.0
4.0
6.0
8.0
10.0
R
(c)
J_ϕ
0.1
0.0
−0.1
2.0
4.0
6.0
8.0
10.0
R
(d)
$(B-B_D)/B_D$
0
−.1
−.2
−.3
−.4
2.0
4.0
6.0
8.0
10.0
R

Fig. 17